ACS Catalysis

pubs.acs.org/acscatalysis Research Article

Effect of the Nuclearity and Coordination of Cu and Fe Sites in β Zeolites on the Oxidation of Hydrocarbons

Petr Sazama,* Jaroslava Moravkova, Stepan Sklenak, Alena Vondrova, Edyta Tabor, Galina Sadovska, and Radim Pilar

Cite This: *ACS Catal.* 2020, 10, 3984−4002 Read Online

ACCESS | Metrics & More | Article Recommendations | Supporting Information

ABSTRACT: Cu and Fe zeolites can activate oxygen for oxidative reactions of methane and stable hydrocarbon molecules. Here, we analyzed the activity of Cu and Fe sites with various nuclearities and coordinations in *BEA zeolites toward complete oxidation of methane, toluene, and ethanol by molecular oxygen. Spectral analysis of the interaction of methane with the individual Cu and Fe sites and a kinetic study show that the oxidation of methane is catalyzed by different active sites with different activation energies. In the low-temperature region (225−325 °C), the activity is primarily caused by reactive bridging oxygen atoms in dimeric Cu and Fe clusters. Isolated Fe^{3+}-oxo ions in the octahedral coordination and Cu^{2+} partially charge-balanced by the framework with less rigid redox states contribute to the activity at higher temperatures of ≥350 °C. The isolated Fe^{3+}-oxo ions tetrahedrally coordinated to the framework oxygen and the bare Cu^{2+} ions charge-balanced exclusively by the framework are strongly stabilized and cannot act as active sites. Oxidation of the hydrocarbons over both the dimeric and isolated Cu and Fe active sites is nonspecific with practically barrierless consecutive reactions of already activated molecules and therefore fully CO_2-selective for all of the hydrocarbons in an excess of oxygen.

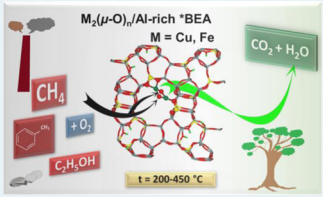

KEYWORDS: *Cu zeolite, Fe zeolite, methane oxidation, methane activation, toluene, ethanol, volatile organic compounds (VOC), organotemplate-free Al-rich beta*

1. INTRODUCTION

The Cu and Fe clusters in zeolites resembling active sites in enzymes have received considerable attention[1−6] because they can activate oxygen, which is potentially useful for partial selective catalytic oxidation of methane.[7] The positively charged clusters of copper and iron ions with specific structures, stabilized by the negative charge of the zeolite framework, can form highly active oxygen species capable of reacting with a strong C−H bond in methane (440 kJ mol^{-1}) at close to room temperatures.[8−10] The activation of molecular oxygen over Cu zeolites was attributed to dinuclear mono- and bis-(μ-oxo) core Cu clusters[1,2,4−6,11−17] and μ-peroxo dicopper[4] or trinuclear μ-oxo[3] clusters mimicking the nuclearity and reactivity of active sites in methane monooxygenases. The catalytic centers responsible for the activity of Fe zeolites were also proposed as various binuclear Fe-oxo cores comprising mono- and bis-(μ-oxo) and (μ-peroxo) species stabilized in the zeolite channels. Although some of the structural features of the Cu and Fe cores, such as the arrangements of oxygen bridge atoms, bond lengths, and positions in three-dimensional (3D) space, may be similar for both zeolites and enzymes, selectivity in partial oxidation of methane is ensured in the enzymes by a complex mechanism including specific ligand fields and the exactly defined environment of the active site, which allow desorption of the product but do not allow further subsequent reactions.[18−21] The chemical behavior of the active site is uniquely suited to methane oxidation in monooxygenases,[22] in contrast to the nonspecific activity of the zeolitic centers. As such complex local structures and functionality are principally lacking in the zeolites, sufficient selectivity can be achieved only in a pseudocatalytic cyclic process with separate sequential steps of (i) oxidation of the di- or trinuclear active centers by molecular oxygen, (ii) oxidation of a hydrocarbon molecule by the activated oxygen bound in the active site, and (iii) desorption of the product, where the hydrocarbon and molecular oxygen are not simultaneously present over the catalyst in any of the steps of the cyclic process. Theoretical and experimental studies have shown that selective oxidation in a true catalytic process with molecular oxygen over zeolites is only possible at very low conversions (≤1%).[17,23] In the presence of molecular oxygen, desorbed oxygen-containing products with weaker C−H bonds are very easily oxidized at a nearby active center and control of the selective oxidation encounters complex difficulties, as it is strongly influenced by the local arrangement and the environment of the active centers in the internal reaction space of the zeolite channels.[17]

This study opens the question of whether the low-temperature oxidation activity of Cu and Fe clusters in zeolites can be

Received: December 16, 2019
Revised: February 23, 2020
Published: February 24, 2020

Downloaded via ACADEMY OF SCIENCES CZECH REPUBLIC on April 3, 2020 at 16:10:26 (UTC).
See https://pubs.acs.org/sharingguidelines for options on how to legitimately share published articles.

ACS Publications © 2020 American Chemical Society

https://dx.doi.org/10.1021/acscatal.9b05431
ACS Catal. 2020, 10, 3984−4002

Table 1. Characteristics of Parent *BEA Zeolites

sample	Si/Al	Si/Al_{FR}	c_{Al} (wt %)	crystal size (nm)	V_{MI} ($cm^3\ g^{-1}$)	surface area ($m^2\ g^{-1}$)	S_{ext} ($m^2\ g^{-1}$)
Al-rich *BEA	4.6	4.8	7.8	300−500	0.19	481	48
Si-rich *BEA	12.7	13	3.3	10−30	0.19	494	66

Table 2. Compositions of Cu-, Fe-, and Pt-*BEA Zeolites and Temperatures for 50, 90, and 98% Conversions in the Complete Oxidation of Methane, Toluene, and Ethanol

sample			ethanol			toluene			
	c_{Fe} (wt %)	Fe/Al	T_{50} (°C)	T_{90} (°C)	T_{98} (°C)	T_{50} (°C)	T_{90} (°C)	T_{98} (°C)	
Al-rich Fe-*BEA	6.05	0.56	201	237	253	295	357	376	
Si-rich Fe-*BEA	3	0.50	208	252	276	295	380	414	
sample			ethanol			toluene			methane
	c_{Cu} (wt %)	Cu/Al	T_{50} (°C)	T_{90} (°C)	T_{98} (°C)	T_{50} (°C)	T_{90} (°C)	T_{98} (°C)	T_{50} (°C)
Al-rich Cu-*BEA	8.7	0.56	216	249	281	264	312	325	407
Si-rich Cu-*BEA	3.04	0.43	210	246	276	326	426	476	
sample			ethanol			toluene			methane
	c_{Pt} (wt %)	Pt/Al	T_{50} (°C)	T_{90} (°C)	T_{98} (°C)	T_{50} (°C)	T_{90} (°C)	T_{98} (°C)	T_{50} (°C)
Al-rich Pt-*BEA	1.44	0.028	192.5	259.4	321.7	223	259	305	450

employed instead of selective oxidation in complete oxidation of hydrocarbons potentially useful for the abatement of emissions of methane and, in general, of volatile organic compounds (VOCs). Deep oxidation of partially oxidized hydrocarbons and oxygen-containing intermediates to carbon dioxide is crucial in the total oxidation of VOCs. Consequently, the lack of selectivity of the enzymelike active centers in zeolites in a standard catalytic oxidation with molecular oxygen could be advantageous for deep oxidation of even stable hydrocarbon molecules. About 80% of VOCs, which belong to the largest contributors to photochemical smog in urban areas, are emitted from motor vehicle exhaust.[24−26] The Cu and Fe clusters active in low-temperature oxidation may be potentially exploited for reducing hydrocarbon emissions from automobile traffic, where zeolites with large adsorption capacities are employed to effectively adsorb unburned heavier VOCs in the so-called "HC reformer trap".[24−26] The active centers in the zeolite could ensure efficient conversion of adsorbed VOCs by deep oxidation when the catalyst reaches the operating temperature. No adequate solution has yet been found for effective catalytic elimination of emissions of methane from natural-gas-fueled vehicles and power generation systems by total oxidation, requiring high temperatures (>400 °C),[27−29] often unattainable in an environmentally and energy-efficient catalytic process. The elimination of emissions of methane remains an important goal for heterogeneous catalysis because of the 20 times larger global warming potential of methane compared to carbon dioxide and significant impact of methane emissions on global warming.[30,31]

In this study, we attempted to design materials with high concentrations of isolated Cu and Fe ions and their clusters with various nuclearities and assessed their reactivity toward methane oxidation. For this purpose, we employed Al-rich β (*BEA) zeolites with very high contents of aluminum in the framework (Si/Al ∼ 5), optimal for binding high concentrations of Fe and Cu ionic species with a versatile redox state and an open coordination sphere,[32,33] which is important for efficient adsorption and oxidation of VOCs.[26] We monitored the formation of individual Cu and Fe ion species in an oxygen-containing atmosphere and analyzed their reactivity toward methane molecules using complementary UV−vis and Mössbauer spectroscopies. The objective was not to develop a catalyst structure for a specific VOC elimination process or analysis of the activity under the diverse, often complicated conditions of different VOC elimination processes but rather to evaluate the redox behavior of various Cu and Fe ion species toward methane oxidation and relate them to the activity of Al-rich Cu- and Fe-*BEA zeolites in model reactions. The study shows that the di- and oligonuclear Fe or Cu ionic centers effectively and selectively catalyze the oxidation of methane, toluene, and ethanol as model VOCs in an O_2-containing atmosphere to form CO_2 and H_2O and that their activities exceed those of most of the supported metal-oxide catalysts.

2. EXPERIMENTAL SECTION

2.1. Preparation of Fe- and Cu-Zeolite Catalysts. The Al-rich *BEA zeolite (Si/Al 4.6) used for the preparation of Fe and Cu catalysts was synthesized by organic-template-free hydrothermal synthesis using seeding with calcined *BEA zeolite (TZB-212, Tricat) and silica (Cabosil) and sodium aluminate as the sources of silicon and aluminum, respectively. The Si-rich *BEA zeolite used for comparing the catalytic properties was kindly provided by Zeolyst International (CP814B-25, Si/Al 12). Characteristics of both zeolites are depicted in Table 1, and details of synthesis and detailed structural characterization of the parent samples are described elsewhere.[33−35] Fe was introduced into the zeolite by ion exchange with an aqueous solution of ferrous sulfate under a nitrogen atmosphere. A total of 1 g of zeolite was added to 50 mL of distilled water at 75 °C in a stirred flask bubbled with nitrogen, with a reflux condenser. A $FeSO_4$ tablet was then added, and the suspension was stirred at 80 °C for 14 h with nitrogen bubbling. The suspension was filtered and washed with demineralized water, and the Fe zeolite was dried under a stream of nitrogen. Copper was introduced into the zeolite by impregnation, followed by solid-phase ion exchange. The dried *BEA zeolite (2 g) was impregnated with 2.28 g of copper nitrate solution of appropriate concentration to obtain Cu/Al ∼ 0.5 and, after drying, calcined in a stream of air at 450 °C for 2 h to form Cu zeolites with dispersed copper oxide particles. The solid-phase ion exchange was then carried out in a stream of ammonia at 340

https://dx.doi.org/10.1021/acscatal.9b05431
ACS Catal. 2020, 10, 3984−4002

°C for 3.5 h, yielding Cu in the cationic sites.[5,36] Platinum was introduced into the Al-rich *BEA zeolite by ion exchange of 1 g of zeolite with 0.03 g of tetraammineplatinum(II) nitrate dissolved in 150 mL of H_2O. After drying, the sample was reduced in a stream of hydrogen at a temperature of 200 °C for 1 h. The compositions of the obtained Cu-, Fe-, and Pt-*BEA zeolite samples are listed in Table 2.

2.2. Structural Analysis. The UV−vis−NIR reflectance spectra of Fe- and Cu-*BEA catalysts in a dehydrated form and heated under air or a methane atmosphere were recorded on a UV−vis−NIR PerkinElmer Lambda 950 spectrometer equipped with an integrating sphere for diffuse-reflectance measurements. The reflectance was recalculated using the Schuster−Kubelka−Munk function. The sample in the form of granules (200−400 μm) was introduced into a quartz U-tube reactor connected with a quartz cuvette and heated to 500 °C under vacuum, with a heating rate of 4.5 °C/min and a delay of 1 h, following which air was introduced for 1 h. After cooling to 250 °C, the reactor was flushed for 1 min with N_2, then CH_4 (3.5% CH_4 in He, 80 mL/min) was introduced for 10 min, followed by flushing with N_2 for 1 min. The spectrum was recorded at room temperature (RT), after which the sample was treated in an air flow at 300 °C for 30 min, flushed for 1 min with N_2, and CH_4 was then introduced for 10 min, followed by flushing for 1 min with N_2. The spectra were recorded after the pretreatment using this procedure with a temperature step of 50 °C up to 500 °C.

The Mössbauer spectra of Fe-*BEA catalysts in a dehydrated form and heated under air or a methane atmosphere were recorded with ^{57}Co in a rhodium matrix as the source of γ-rays, where an α-Fe foil was used as a reference. Samples in the form of self-supporting discs were directly transferred between the reaction chamber and the measuring position. MossWinn software was used for the spectral deconvolution into Lorentzian-shaped components. Prior to measurements, the sample was heated to 500 °C under vacuum with a heating rate of 4.5 °C/min and a delay of 1 h; air was then introduced for 1 h. After cooling to 250 °C, the reactor was evacuated, after which CH_4 was introduced for 10 min, followed by brief evacuation. The spectrum was recorded at RT. The whole procedure was repeated with the interaction of the sample with methane at 400 °C.

H_2-TPR profiles of Cu- and Fe-*BEA zeolites were measured with a Micromeritics AutoChem 2950 HP Chemisorption analyzer. Each sample was first treated in a quartz reactor at 450 °C for 30 min under O_2 (with a flow rate of 10 mL/min), followed by cooling down to 50 °C. After signal stabilization, the samples were heated from 50 to 1000 °C with a heating rate of 10 °C min^{-1} in a H_2/Ar stream (10 vol % H_2) with a flow rate of 20 mL min^{-1}. A JEOL JEM-2100Plus high-resolution transmission electron microscope operated at 200 kV (LaB_6 cathode, point resolution 1.9 Å) was used to obtain high-resolution transmission electron microscopy (HR-TEM) images for analysis of Pt dispersion in an Al-rich Pt-*BEA catalyst (Figure S1).

2.3. Computational Models and Methods. *2.3.1. Computational Models.* The calculations were carried out to model structures whose general spectral features were observed during spectroscopic analysis, to obtain more complete information about their possible structures. Calculations were not performed to determine all of the possible configurations of the Cu and Fe species that could theoretically occur. The calculated metal-oxo species were modeled as the mono(μ-oxo)dicopper, bis(μ-oxo)dicopper, bis(μ-oxo)diiron, (μ-oxo)(μ-peroxo)diiron, and additional Fe-oxo structures in the Al-rich *BEA zeolite sample with the known Al distribution.[33] The starting orthorhombic structure was downloaded from the zeolite structural database: http://www.iza-structure.org/databases/. Three models were employed for the copper species and five models for the iron-oxo cations. All eight models possess P1 symmetry and feature one unit cell of the *BEA zeolite with 10 Al/Si substitutions (i.e., the Si/Al ratio is 5.4). The Al distribution of the Al-rich *BEA zeolite was determined in our previous study.[33] The Al atoms that do not balance iron-oxo or copper-oxo species are compensated by protons located on one of the four O atoms of the corresponding AlO_4^- tetrahedra.

The Fe_A and Fe_B models feature one $[Fe(II)]^{2+}$ cation accommodated in the β cationic site balanced by two Al(T3) atoms [i.e., Al(T3)−Si−Si−Al(T3) sequence] and one $[Fe(III)O]^+$ species balanced by one Al(T2) and Al(T4) atom, respectively. The difference between the Fe_A and Fe_B models is that the Al(T3) and Al(T2) atoms are separated by one *Si* atom [i.e., Al(T3)−Si−Si−Al(T3)−*Si*−Al(T2)] and the Al(T3) and Al(T4) atoms by two *Si* atoms [i.e., Al(T3)−Si−Si−Al(T3)−*Si*−*Si*−Al(T4)].

The Fe_C, Fe_D, and Fe_E models possess two $[Fe(III)O]^+$ species, each balanced by one Al atom, forming an Al(T4)−Si−Si−Si−Al(T5) sequence. The two $[Fe(III)O]^+$ species either create bis(μ-oxo)diiron species (Fe_C model) or include one additional O atom to yield the (μ-oxo)(μ-peroxo)diiron structure (Fe_D model) and (μ-oxo)diiron (Fe_E model) species with two additional O atoms.

The Cu_A, Cu_B, and Cu_C models include two Cu cations, each balanced by one Al atom, forming an Al(T4)−Si−Si−Si−Al(T5) sequence. The two Cu cations form a (μ-oxo)dicopper structure in the Cu_A model, bis(μ-oxo)dicopper species in the Cu_B model, and two Cu(I) cations in the Cu_C model.

2.3.2. Electronic Structure Calculations. Periodic density functional theory (DFT) calculations were carried out by employing the Vienna Ab initio simulation package (VASP) code.[37−40] The spin state S (S = N/2; N is the number of unpaired electrons) of the ground state for each computational model was determined from the atomic composition of the model and the oxidation state of the Cu and Fe atoms. The number of unpaired electrons (i.e., the spin state) was fixed during the molecular dynamics (MD) simulations and optimizations. Moreover, for the most stable optimized structure for all of the computational models, the spin state used was verified that it really corresponds to the ground state. The Kohn−Sham equations were solved variationally in a plane-wave basis set using the projector-augmented wave (PAW) method of Blöchl,[41] as adapted by Kresse and Joubert.[42] The exchange-correlation energy was described by the Perdew−Burke−Ernzerhof (PBE) generalized gradient approximation (GGA) functional.[43] Brillouin zone sampling was restricted to the Γ point. A plane-wave cutoff of 600 eV and the dDsC dispersion correction[44,45] were used for geometry optimizations, and a smaller cutoff of 400 eV and the DFT-D2 method[46] were used for the molecular dynamics simulations.

2.3.3. Molecular Dynamics. The molecular dynamics (MD) simulations were carried out on all of the five Fe models and the Cu_A, Cu_B, and Cu_C models. The lattice parameters were fixed at their experimental values during the MD calculations for all of the models. The MD computations used the exact Hellmann−Feynman forces acting on atoms and applied the statistics of the canonical ensemble to the motion of the atomic nuclei[47] using the Verlet velocity algorithm[48,49] to integrate Newton's

https://dx.doi.org/10.1021/acscatal.9b05431
ACS Catal. 2020, 10, 3984−4002

equations of motion. The time step for the integration of the equations of motion was 1 fs. The simulations were run for 10 000 fs at 400 K. Visual inspection of the structures along the MD trajectories showed that the duration of the MD simulations was sufficient because it included both the rearrangements of the local structures of the zeolite framework (up to ca. 3 000 fs) and a long period (ca. 7 000 fs) when the system fluctuated around equilibrium and "snapshots" were collected and optimized. Similar time lengths were used for MD simulations of the cationic sites in zeolites.[33,50−55] The MD simulations served to obtain the rearranged local structures (details are provided in our prior studies[50,51]). No physical quantity is derived from the MD trajectories.

2.3.4. Geometry Optimizations. The structures of 20 distinct snapshots collected at 500, 1000, 1500, ..., 10 000 fs of the MD simulations were optimized for all of the computational models. The most stable structure for each model is used. The atomic positions were optimized at constant volume by employing a conjugate-gradient algorithm minimization of energies and forces, where the lattice parameters were fixed at their experimental values.

2.3.5. Comparison of the Relative Stabilities of the Computational Models. The relative stabilities of the models were compared using the approach described in ref. 94. Technical details are provided in the Supporting Information.

2.4. Analysis of Catalytic Activity. Activities in oxidation of methane, toluene, and ethanol were measured in a quartz tube gas-flow reactor with an amount of the granulated (200−400 μm) sample of 140 mg, at a total gas flow rate of 75 mL/min at atmospheric pressure corresponding to GHSV 20 000 h^{-1}. The activity was measured after activation in air for 1 h at 450 °C. Methane oxidation was measured in the reaction stream containing 1 000 ppm methane and 21% oxygen in helium in the temperature range from 450 °C gradually decreasing to 50 °C. The influence of external mass and heat transfer under the reaction conditions of methane oxidation was excluded by experiments that varied the total gas flow and the weight of the catalyst at constant values of GHSV, in which the conversions of methane were constant. The crystal sizes of the parent zeolites ∼0.05−0.4 μm guaranteed the absence of intracrystalline diffusion constraints, as shown in preceding studies for reactions at temperatures below 500 °C. The influence of intragrain diffusion constraints was excluded by the experiment with catalyst grains whose dimensions were varied from 0.1 to 0.4 mm. For measurements of oxidation of ethanol (250 ppm) or toluene (180 ppm), the flow of helium of 60 mL/min was saturated with the vapors in a cooled saturator (−19 °C) and mixed with a flow of oxygen of 15 mL/min. The reaction products were analyzed by gas chromatography (GC Hewlett-Packard 5890). Columns of an HP-Plot Q (30 m × 0.53 mm × 40 μm film thickness) and a molecular sieve 5 A (30 m × 0.53 mm × 25 μm film thickness) were used for the separation of N_2, O_2, CO, and CO_2 analyzed with a thermal conductivity detector.[56] Hydrocarbons were separated on an HP-Plot Q (30 m × 0.53 mm × 40 μm film thickness) and monitored by a flame ionization detector (FID).

3. RESULTS

3.1. Reducibility of Cu and Fe Sites. Figure 1 shows the H_2-TPR profiles of the Al-rich Cu- and Fe-*BEA zeolites pretreated in air at 500 °C. For the Fe zeolite, the TPR curve contained a broad peak of hydrogen consumption at 200−450 °C and high-temperature reduction above 750 °C. The high-temperature peak reflects reduction of highly stabilized single bare Fe^{2+} ions coordinated to the zeolite framework, which can be reduced above 600 °C.[57,58] The broad peak of hydrogen consumption at 200−450 °C is associated with the reduction of isolated Fe^{3+}-oxo species and Fe^{3+}-oxo dimers and oligomers, while single Fe(III) ions without a ligand cannot be coordinated in the zeolitic channels due to the lack of the local negative charge requiring three close Al atoms.[57] The pattern of the broad reduction peak reveals that it consists of several superimposed peaks reflecting Fe^{3+} species with a different reductivity. The reduction with a shoulder appearing from 200 to 300 °C can be associated with Fe(III)-oxo species of high reactivity previously assigned to highly reactive oligomeric species partially charge-balanced by the zeolite framework.[57] The signal at 300−550 °C reflects difficult-to-reduce Fe(III)-oxo species.

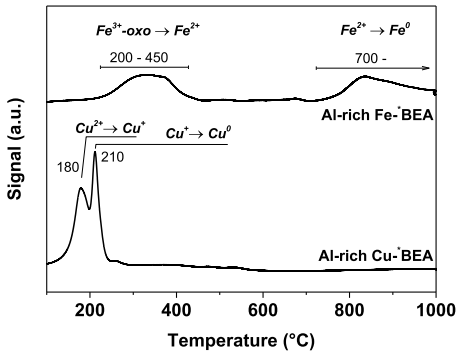

Figure 1. H_2-TPR profiles of the Al-rich Cu- and Fe-*BEA zeolites pretreated in air at 500 °C.

The H_2-TPR profile of Al-rich Cu-*BEA shows two reduction peaks at 180 and 210 °C, which reflect the reduction of Cu^{2+} in two steps from Cu^{2+} to Cu^{+} and Cu^{+} to Cu^{0} present in mononuclear Cu(II) or more complex polynuclear Cu(II) species charge-compensated by the zeolite framework.[59,60] The very low temperature for the reduction and the absence of a significant reduction at 250−300 °C characteristic of supported copper oxides[60,61] indicate the presence of Cu^{2+} in a highly dispersed form with high reactivity and versatile redox behavior.

3.2. UV−vis Analysis of the Reactivity of Cu and Fe Sites with Methane. To analyze the reactivity of isolated and dimeric and oligomeric Cu and Fe species toward methane oxidation, the changes in speciation of Cu and Fe in the air-activated Al-rich Cu- and Fe-*BEA samples after exposure to methane at various temperatures were investigated by UV−vis−NIR spectroscopy. Figure 2 shows the UV−vis−NIR spectrum of the air-activated Al-rich Cu-*BEA catalyst and those after subsequent exposure to flows of methane at temperatures of 250−500 °C. With Al-rich Cu-*BEA exposed to a stream of air, intense absorption bands at 13 400 cm^{-1} due to the d−d electronic transitions of Cu^{2+} ions and at 40 200 and 47 300 cm^{-1} corresponding to O → Cu^{2+}/Cu^{+} charge transfer, along with low intensity of the absorption bands at 22 500 and 28 700 cm^{-1}, attributed to a small number of dimeric Cu sites,[11,62] were observed. A smaller amount of the dimeric Cu species compared to Cu-MOR[12,62] and Cu-ZSM-5[11,63] is typical of Cu-*BEA zeolites.[64] The band at 28 700 cm^{-1} was assigned in the literature to μ-(η^2:η^2)peroxo dicopper(II) ($[Cu_2(O_2)]^{2+}$),[64−66] while the band at 22 500 cm^{-1} was attributed to a mono-(μ-oxo)dicopper(II) complex ($[Cu_2(\mu\text{-}O)]^{2+}$)[5,11,64] or bis($\mu$-oxo) dicopper ($[Cu_2(\mu\text{-}O)_2]^{2+}$).[1,14] The precise specification of the structure of the dimeric Cu species on a molecular level is the

https://dx.doi.org/10.1021/acscatal.9b05431
ACS Catal. 2020, 10, 3984−4002

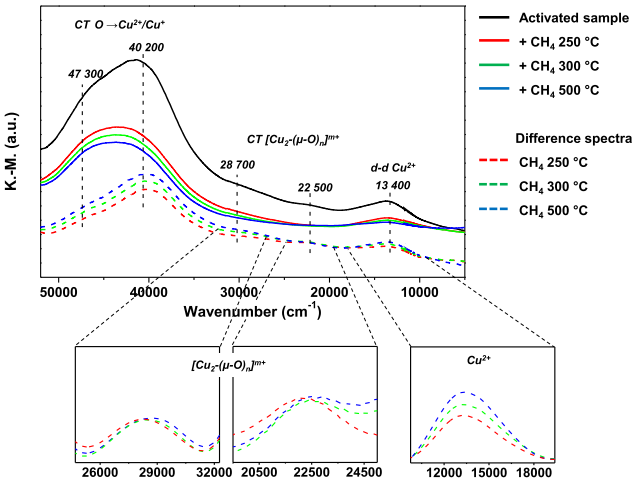

Figure 2. UV−vis−NIR spectra of the Al-rich Cu-*BEA zeolite activated in an air flow at 500 °C and after interaction with CH_4 at 250−500 °C. The dimeric copper species $[Cu_2\text{-}(\mu\text{-}O)_n]^{m+}$ already interact completely with CH_4 at 250 °C, while reduction of isolated Cu^{2+} ions proceeds up to 500 °C.

subject of unceasing discussions,[2−4,6,11,14,16,60,63,64,66−69] but no agreement has been reached. Determination of the exact structure of the dimer Cu cores representing a small part in the heterogeneous Cu system is not experimentally achievable; therefore, we performed calculations showing possible stable Cu structures in an Al-rich *BEA zeolite (see Section 3.4). The addition of methane at 250 °C resulted in the disappearance of the bands at 22 500 and 28 700 cm^{-1} and in a decrease in the intensity of the bands at 13 400, 40 200, and 47 300 cm^{-1}. The disappearance of the bands at 22 500 and 28 700 cm^{-1} and the decrease in the spectral intensity at 13 400 cm^{-1} indicate the reaction of dimeric Cu sites with methane and the reduction of participating divalent Cu^{2+} ions. The formed Cu^+ ions have a fully occupied d shell ($3d^{10}$) and do not provide any d−d transitions. These findings are in agreement with the observation of high reactivity of Cu cores in Cu-ZSM-5,[11,63] Cu-MOR,[12,62] and Cu-SSZ-13.[4] The exposure of the Cu-*BEA catalyst to methane at higher temperatures resulted in a progressive decrease in the intensity of the bands at 13 400 cm^{-1} and at 40 200 and 47 300 cm^{-1}, indicating the reduction of isolated Cu^{2+} ions present in the cationic sites of the zeolite. While the different spectra clearly indicate a completed reaction of all of the oxygen-bearing Cu dimers with a methane molecule already at 250 °C, isolated Cu^{2+} ions at the cationic positions of the zeolite may react with methane at 300−500 °C, while some of these ions do not interact with methane even at 500 °C. Isolated Cu^{2+} ions are located in the plane or slightly above the plane of the framework oxygens in six-membered rings[64,66,69] with geometry and redox properties affected by the presence of one or two Al atoms in the close vicinity[66−68] in dehydrated zeolites. Our previous study on an Al-rich Cu-*BEA catalyst[32] indicated the presence of two groups of isolated Cu^{2+} cations: (i) strongly stabilized bare Cu^{2+} coordinated only to framework oxygens bound in the cationic sites and balanced mostly by the charge of two Al atoms in the framework in Al−O−(Si−O)$_2$−Al sequences and (ii) Cu^{2+} ions capable of fast conversion between Cu^{2+} and Cu^+, compensated by the charge from one aluminum atom from the Al−O−(Si−O)−Al sequence crossing the wall between two neighboring 12-ring channels. The later Cu^{2+} ions, partially charge-balanced by the framework and another ligand, such as the OH group, can provide higher redox activity compared to bare Cu^{2+} cations.[32,70] The results of UV−vis analysis clearly show the heterogeneity of the Cu species and their different redox behaviors. The most active Cu sites bearing an active oxygen are represented by dimeric Cu clusters followed by reducible isolated Cu^{2+} ions partially charge-compensated by the negative charge of the zeolite framework. Part of the Cu^{2+} ions remain highly stabilized in the cationic sites and do not react with methane even at 500 °C.

Figure 3 depicts the UV−vis−NIR spectra of the Al-rich Fe-*BEA zeolite after activation in air at 500 °C and after

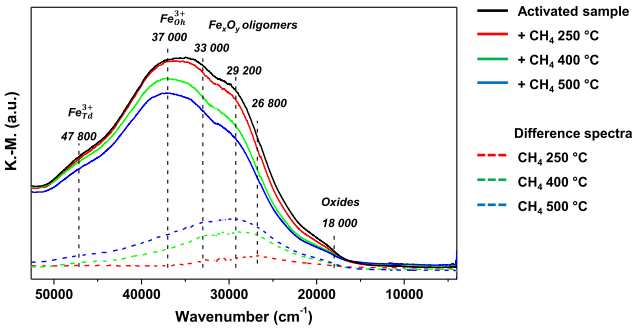

Figure 3. UV−vis−NIR spectra of the Al-rich Fe-*BEA zeolite activated in an air flow at 500 °C and after interaction with CH_4 at 250−500 °C. The dimeric and oligomeric Fe_xO_y species interact with CH_4 at much lower temperatures compared to isolated Fe^{3+}_{Oh} and Fe^{3+}_{Td} ions.

subsequent interaction with methane at 250−500 °C. The spectrum of the activated Fe zeolite is characterized by wide absorption bands ranging from near infra-red (NIR) to UV, showing the heterogeneity of the Fe^{3+} species, as also indicated by the H_2-TPR results; this is typical of zeolites with higher iron loading.[57,71] The very low intensity of the absorption edge at 18 000 cm^{-1} corresponding to Fe oxides[72,73] and very high intensity of the bands in the UV region characteristic of charge-transfer transitions (O → Fe^{3+}) in oligonuclear and isolated Fe^{3+} species[71,74,75] indicate the presence of a large amount of well-dispersed Fe without any significant presence of iron oxides. The absorption bands from 20 000 to 33 000 cm^{-1} can be assigned to various Fe_xO_y oligomers with a frequency reflecting their local coordination and nuclearity.[71,74,75] An increasing number of Fe−O bonds with increasing nuclearity in the Fe^{3+}-oxo oligomers can result in a shift in the energy of the CT transition to lower values.[72] The absorptions at about 28 000−33 000 cm^{-1} were assigned in the literature to dinuclear Fe^{3+}-oxo complexes; however, the absorptions at 20 000 to 33 000 cm^{-1} can also reflect other defined polynuclear Fe^{3+}-oxo complexes, where the lower-energy bands at about ≤25 000 cm^{-1} indicate the presence of larger Fe^{3+}-oxo oligomers.[57,71,72,74,75] The isolated iron ions are manifested in the absorption bands at 37 000 and 47 800 cm^{-1}, characteristic of the octahedral and tetrahedral coordination of Fe^{3+}-oxo, respectively.[57,74,76]

The characteristic absorption peak of dimeric/oligomeric Fe-oxo species at 28 000−33 000 cm^{-1} decreased in intensity after the catalyst was exposed to methane at 250 °C, indicating reduction of the Fe^{3+} ions and interaction of the oxygen in the dimeric/oligomeric species with methane. When the temperature was increased to 400 °C, a further decrease in the intensity of the band of the dimeric/oligomeric Fe-oxo species at 28 000−33 000 cm^{-1} and a concomitant decrease in the intensity of the absorption at 37 000 cm^{-1} of isolated octahedral Fe^{3+}-oxo were

https://dx.doi.org/10.1021/acscatal.9b05431
ACS Catal. 2020, 10, 3984−4002

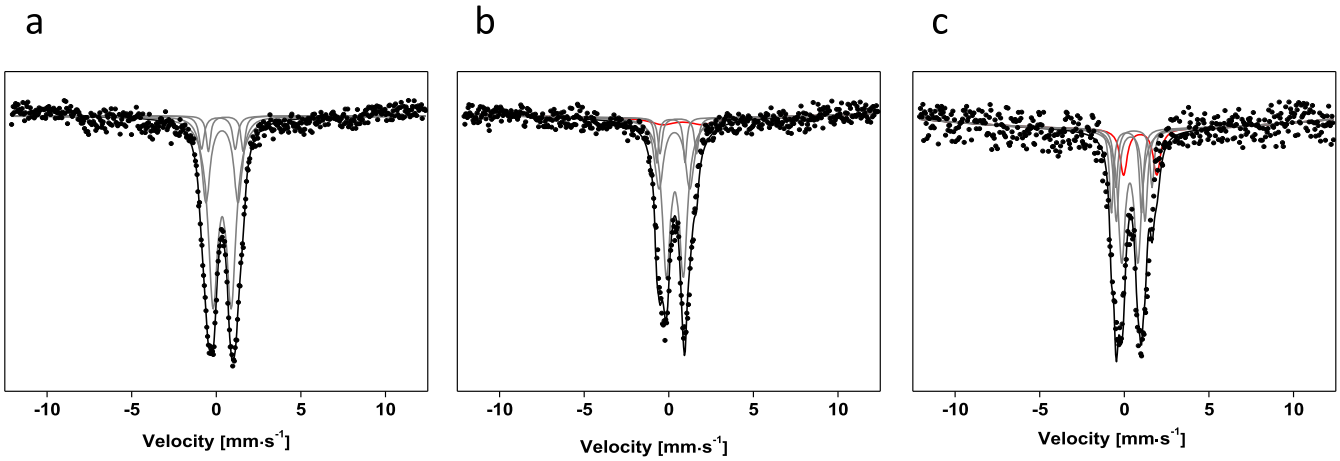

Figure 4. Mössbauer spectra of the Al-rich Fe-*BEA zeolite activated in (a) air at 500 °C followed by interaction with methane at (b) 250 and (c) 400 °C; Fe^{3+} components are in gray, and Fe^{2+} components are in red.

observed. When the temperature was raised to 500 °C, the absorption band at 47 800 cm^{-1}, characteristic of tetrahedral coordination of Fe^{3+}-oxo, also began to decrease in intensity. The observed spectral changes in the Fe^{3+} moieties after interaction with methane at the different temperatures show that the nuclearity and coordination of Fe^{3+} ions in the zeolite channels dramatically affect their redox behavior. Dinuclear/oligonuclear Fe^{3+}-oxo complexes are the most active sites with the ability to react with methane at temperatures as low as 250 °C. In contrast, the isolated octahedral Fe^{3+}-oxo partially charge-balanced by the charge of the zeolite framework are much less reactive, interacting with methane at temperatures of about 400 °C. The tetrahedral coordination of isolated Fe^{3+}-oxo ions to the zeolite framework greatly stabilizes their redox state and allows the reaction at a temperature of about 500 °C. This is consistent with the results of H_2-TPR analysis, which showed both easily reducible Fe^{3+} bearing an oxygen ligand with the ability to also react with hydrogen at low temperatures and difficult-to-reduce Fe^{3+}-oxo species.

3.3. Mössbauer Analysis of the Reactivity of Fe Sites with Methane. Mössbauer spectroscopy was used as a complementary technique for analysis of the valence state and structure of Fe species in the Al-rich Fe-*BEA zeolite and changes in the oxidation state and coordination of the Fe species after their interaction with methane at 250 and 400 °C. The Mössbauer spectra are depicted in Figure 4, and the isomer shift (IS) and quadrupole splitting (QS) parameters reflecting the oxidation state and coordination are presented in Table 3. The components characterized by IS values from 0.1 to 0.6 $mm \cdot s^{-1}$ were assigned to Fe^{3+} ions and components with IS values higher than 0.7 $mm \cdot s^{-1}$ were ascribed to Fe^{2+} ions in accordance with the previously reported data on Fe zeolites.[72,77−85] The best fitting parameters were obtained when the spectrum of the oxidized Al-rich Fe-*BEA zeolite was deconvoluted using four components A−D, describing Fe^{3+} with different coordinations. Component A is characterized by IS 0.32−0.36 $mm \cdot s^{-1}$, which is between typical IS values for tetrahedral (IS < 0.3 $mm \cdot s^{-1}$) and for octahedral or five-coordinated Fe^{3+} ions (IS > 0.3),[77] and by QS ∼ 1 $mm \cdot s^{-1}$, which indicates symmetry distortion in the ligand field of the Fe^{3+} ion. Dubkov et al.[77] assigned components with IS ∼ 0.4 and QS ∼ 0.8−1 $mm \cdot s^{-1}$ to dinuclear Fe^{3+} species formed after oxidative treatment of Fe-ZSM-5 zeolites. The IS and QS parameters similar to those of component A were found for μ-hydroxo di-bridged Fe^{3+} species.[86] The predominant presence of component A (62%) in the spectrum of the Al-rich Fe-*BEA zeolite is consistent with the observation of the formation of Fe dimers in Fe zeolites of various structures with higher Fe loadings[87−89] and easy formation of the binuclear Fe clusters previously described in Si-rich Fe-*BEA zeolites.[90] However, it should be noted that this component may include a number of similar Fe^{3+} species, depending on the position and spatial arrangement in the zeolite channel and the particular arrangement of O and OH ligands, as the theoretical calculations (see Section 3.4) and the broad adsorption bands in the UV−vis spectra (Figure 3) suggest the possibility of the formation of a wide variety of local configurations for the dimeric Fe^{3+} ions. The IS and QS parameters of component B are consistent with those of the tetrahedrally coordinated Fe^{3+} ion, also observed as minor fractions in UV−vis spectra as the absorption band at 47 800 cm^{-1}. Components C and D can be assigned to extraframework Fe^{3+} species with octahedral oxygen ligancy and a low symmetry. The presence of these octahedral coordinated

Table 3. Analysis of Fe Species in Al-Rich Fe-*BEA by Mössbauer Spectroscopy. Isomer Shift (IS), Quadrupole Splitting (QS), and Spectral Contribution after Oxidation with O2 and Interaction with Methane at Different Temperatures

treatment	component	IS ($mm \cdot s^{-1}$)	QS ($mm \cdot s^{-1}$)	rel. (%)	Fe species
air at 500 °C	A	0.34	0.97	62	Fe^{3+} Td/Oh
	B	0.12	1.80	6	Fe^{3+} Td
	C	0.55	2.05	6	Fe^{3+} Oh
	D	0.33	1.89	26	Fe^{3+} Oh
+ CH_4 at 250 °C	A	0.36	1.01	54	Fe^{3+} Td/Oh
	B	0.12	1.67	7	Fe^{3+} Td
	C	0.56	2.16	6	Fe^{3+} Oh
	D	0.35	1.81	26	Fe^{3+} Oh
	E	0.81	2.35	7	Fe^{2+} Oh
+ CH_4 at 400 °C	A	0.32	0.96	40	Fe^{3+} Td/Oh
	B	0.12	1.77	14	Fe^{3+} Td
	C	0.56	2.13	10	Fe^{3+} Oh
	D	0.37	1.71	21	Fe^{3+} Oh
	E	0.93	1.99	15	Fe^{2+} Oh

https://dx.doi.org/10.1021/acscatal.9b05431
ACS Catal. 2020, 10, 3984−4002

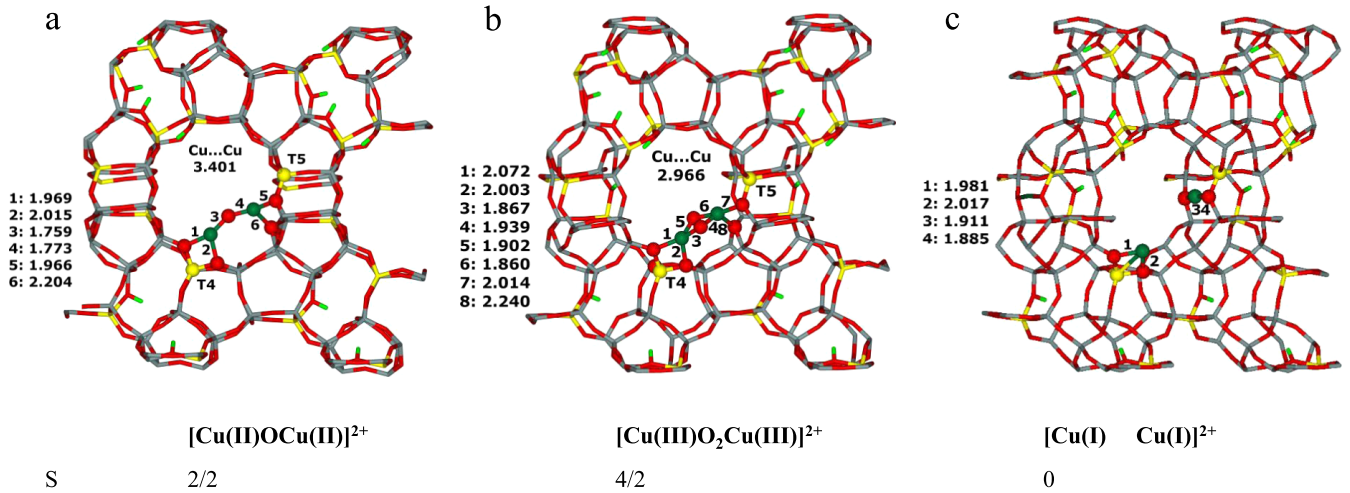

	[Cu(II)OCu(II)]$^{2+}$	[Cu(III)O$_2$Cu(III)]$^{2+}$	[Cu(I) Cu(I)]$^{2+}$
S	2/2	4/2	0

Figure 5. Possible structures of Cu and Cu-oxo species located in accessible 12-ring channels and charge-compensated by a typical Al(T4)−Si−Si−Si−Al(T5) sequence in the Al-rich *BEA. The optimized structures after the DFT molecular dynamics simulations for (a) Cu_A model of (μ-oxo)dicopper ($[Cu_2(\mu\text{-}O)]^{2+}$), (b) Cu_B model of bis(μ-oxo)dicopper ($[Cu_2(\mu\text{-}O)_2]^{2+}$), and (c) Cu_C model of Cu ions coordinated exclusively to the framework oxygens. The distances are in Å. Silicon atoms are in gray, oxygen atoms in red, aluminum atoms in yellow, and copper atoms in green. The spin state is denoted S.

Fe^{3+} ions is reflected in an intense absorption band at about 37 000 cm^{-1} in the UV−vis spectra.

A new component E with IS 0.81 characteristic of Fe^{2+} ions appeared in the Mössbauer spectra after interaction with methane at 250 °C. A simultaneous decrease in the relative proportion of component A indicates that interaction with methane led to the partial reduction of Fe^{3+} in dimeric species to Fe^{2+} and that an active oxygen ligand reacted with the methane molecule. No changes were observed in the intensity of the B−D components representing other forms of Fe^{3+} at 250 °C within the accuracy of the method. An increase in the temperature to 400 °C resulted in an increase in the intensity of component E to 15%, a significant decrease in component A, and a decrease in component D. The observed changes in the spectrum are consistent with the continued reaction of methane with oxygen ligands/bridges in Fe^{3+} dimers and a new interaction of octahedrally coordinated Fe^{3+} resulting in their reduction to Fe^{2+}. Minor differences in the IS and QS parameters of the E component resulting from the reaction at 250 and 400 °C indicate the formation of Fe^{2+} ions with some differences in their local arrangement due to the differences in the local arrangement of the original Fe^{3+} sites. A slight increase in the intensity of components B and C after the interaction with methane at 400 °C could be explained by changes in the coordination of one of the Fe^{3+} in the dimer after interaction with methane. Analogously, Kim et al.[90] showed by in situ spectroscopic analysis that some of the Fe−O−Fe species in Fe-*BEA underwent a reversible structural transformation of dimeric and isolated Fe^{3+} upon heating and interaction with a reducing agent under SCR conditions. The results of the Mössbauer analyses complement and support the results of the UV−vis analysis and together show that some of the hydroxo/oxo-di/bridged Fe^{3+} and Fe^{3+} Oh ions are capable of redox interaction with a methane molecule at ∼250 and ∼400 °C, respectively, while isolated Fe^{3+} Td do not undergo redox changes.

3.4. Computational Models of the Structure of Dinuclear Cu and Fe Sites. The great complexity and versatility of Cu and Fe structures lead to uncertainties on the nuclearity and structure of the active core even in the case of methane monooxygenase.[91−93] An unambiguous structural characterization of the dimeric Cu and Fe species is even more difficult to achieve for Fe/Cu-zeolitic catalysts due to the heterogeneity of the sites with different nuclearities and versatilities in the redox state under the different conditions. Experimental spectral methods that could accurately describe the structure are not applicable in the presence of several similar Fe or Cu moieties in unspecified proportions. Therefore, we used periodic DFT calculations with extensive MD simulations that can indicate the possible structure of dimeric species accommodated in the Al-rich *BEA zeolite. Calculated dimeric species were coordinated to the framework rings with the known Al distribution in the Al-rich *BEA zeolite sample determined in our previous study,[33] which indicated the predominant occurrence of close unpaired Al atoms (66%) linked with an Al−Si−Si−Si−Al sequence.[54] The Al−Si−Si−Si−Al sequence located on a wall of the 12-ring channel was chosen to accommodate a dimeric site accessible for reactants. The calculated structures of possible dimeric metal-oxo species were modeled on the basis of previous studies of related Fe- and Cu-zeolite systems. The activation of molecular oxygen over Cu zeolites was attributed in the literature to the dinuclear mono(μ-oxo)dicopper core ($[Cu_2\text{-}(\mu\text{-}O)]^{2+}$)[4−6,11−13] and the bis(μ-oxo)dicopper core ($[Cu_2\text{-}(\mu\text{-}O)_2]^{2+}$).[1,2,13−16] These models were employed for the calculation. The calculations of the mono(μ-oxo)dicopper (Cu_A model, Figure 5a) and bis(μ-oxo)dicopper (Cu_B model, Figure 5b) species indicated the distance between the two Cu atoms to be 3.401 and 2.966 Å, respectively. The ground states were computed to be S = 2/2 and 4/2, respectively, and the Cu oxidation states were 2 and 3, respectively. Similarly, as for the bis(μ-oxo)diiron structure, there is no "α oxygen-like" atom in the structure. The bridging oxygen atoms could be responsible for the oxidative properties of the system. All our attempts to optimize the structure of the (μ-peroxo)dicopper species analogous to complex 6 in ref65 failed. The optimizations yielded structures identical to those of the Cu_B model. Therefore, we assumed that the (μ-peroxo)-dicopper structure does not correspond to a minimum on the potential energy surface. This result is consistent with the fact that complex 6 in ref65 is not thermally stable.

https://dx.doi.org/10.1021/acscatal.9b05431
ACS Catal. 2020, 10, 3984−4002

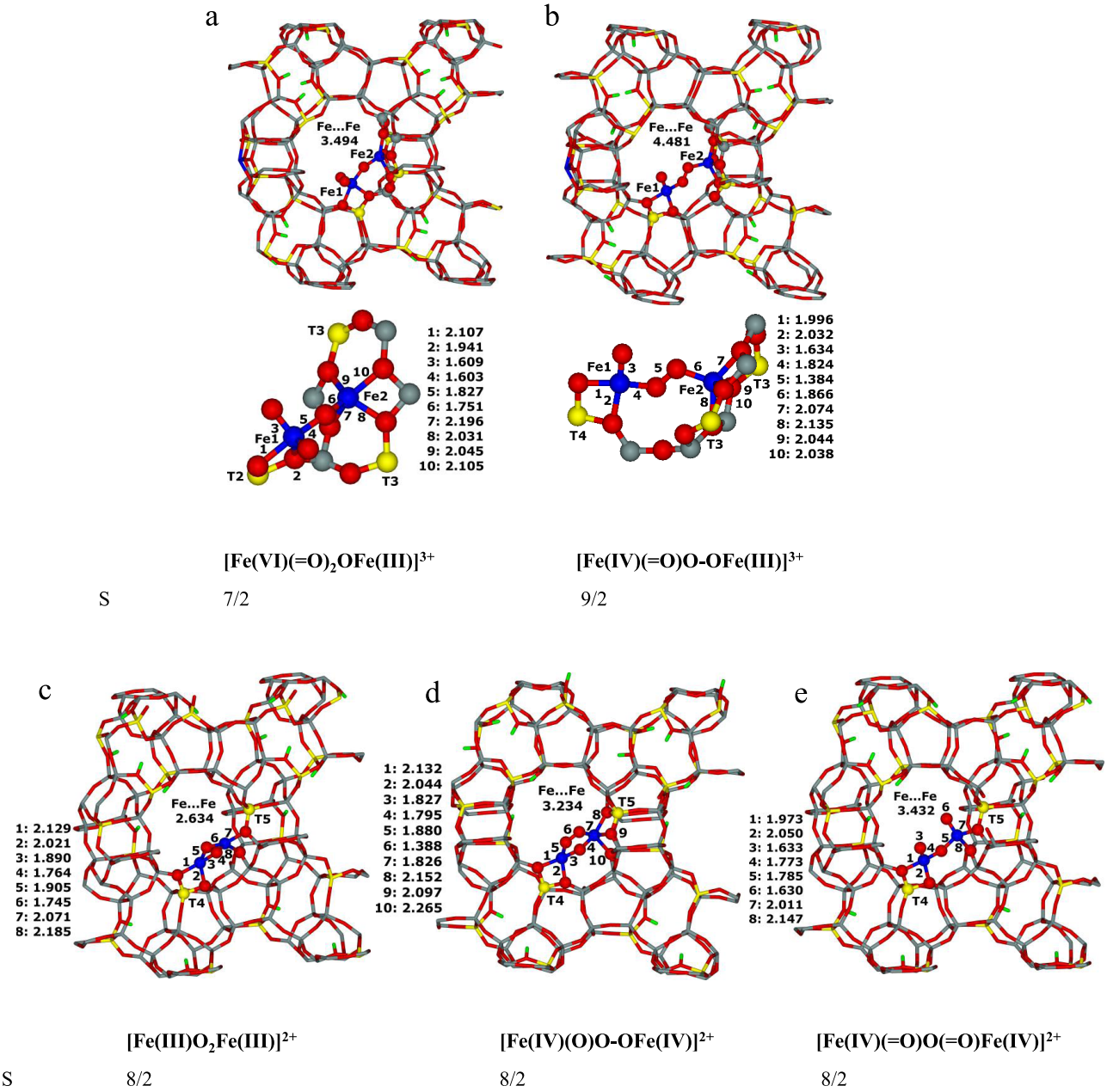

Figure 6. Possible structures of Fe-oxo species located in accessible 12-ring channels. The optimized structures after the DFT molecular dynamics simulations for (a) Fe_A model charge-compensated by an Al(T3)−Si−Si−Al(T3) sequence and Al(T2), (b) Fe_B model balanced by an Al(T3)−Si−Si−Al(T3) sequence and Al(T4), (c) Fe_C model, (d) Fe_D model, and (e) Fe_E model, with all of the three models (c−e) charge-compensated by Al(T4)−Si−Si−Si−Al(T5). The distances are in Å. Silicon atoms are in gray, oxygen atoms in red, aluminum atoms in yellow, and iron atoms in blue. The spin state is denoted S.

Our calculations of the relative stabilities (Table S1) show that the mono(μ-oxo)dicopper site (the Cu_A model) is more stable by 29 kcal/mol than the bis(μ-oxo)dicopper cluster (the Cu_B model) in the Al-rich *BEA zeolite similarly as in the ZSM-5 zeolite, while the opposite is found for mordenite.[94,95] Both the mono(μ-oxo)dicopper and the bis(μ-oxo)dicopper clusters are more stable than the unoxidized Cu(I) cations (the Cu_C model) by 41 and 12 kcal/mol, respectively, indicating the tendency of Cu(I) cations exchanged in the Al-rich *BEA zeolite to form oxidized bridges.

As the partial oxidation of methane over Fe-exchanged zeolites was associated with various di-iron core structures,[9,10,21] five models for the dinuclear iron cations with μ-oxo and μ-peroxo ligands were calculated. The Fe_A model (Figure 6a) yielded a structure in which the Fe1 atom features two oxygen atoms forming double bonds to Fe1 (the calculated bond lengths are 1.603 and 1.609 Å). These two O atoms resemble the α oxygen atom,[50,55,96,97] and it is probable that they could be responsible for the oxidative properties of the system. The distance between the two Fe atoms is 3.494 Å and therefore they are connected by a μ-oxo bridge. The ground state is calculated to correspond to S = 7/2. The formal oxidation states of Fe1 and Fe2 are 6 and 3, respectively. Therefore, the Fe1 atom corresponds to the Fe atom of ferrate(VI) ($Fe^{VI}O_4^{2-}$).[98]

The computational results regarding the Fe_B model (Figure 6b) indicate a structure in which the Fe1 atom possesses one

https://dx.doi.org/10.1021/acscatal.9b05431
ACS Catal. 2020, 10, 3984−4002

oxygen atom forming double bonds to Fe1 (the calculated bond length is 1.634 Å). In addition, this O atom resembles the α oxygen atom[50,55,96,97] and could be linked to the oxidative properties of the system. The Fe1 and Fe2 atoms are connected by a μ-peroxo bridge due to a larger distance between the two Fe atoms (4.481 Å). The ground state is computed to be related to S = 9/2. The formal oxidation states of Fe1 and Fe2 are 4 and 3, respectively.

Comparison of $[Fe(VI)(=O)_2OFe(III)]^{3+}$ (the Fe_A model) and $[Fe(IV)(=O)O-OFe(III)]^{3+}$ (the Fe_B model) reveals that the former is slightly more stable by 4 kcal/mol that the latter. However, it should be noted that the Al distribution and the Al siting, and not solely thermodynamics, determine which structure is formed. The $[Fe(VI)(=O)_2OFe(III)]^{3+}$ structure cannot be formed when the Al(T3)−Si−Si−Al(T3) sequence and the Al(T4) atom compensate the $[Fe_2O_3]^{3+}$ species due to a larger distance between the two Fe atoms (4.481 vs 3.494 Å; Figure 6).

By employing DFT calculations, Li et al. found that two close $[FeO]^+$ species readily form one bis(μ-oxo)diiron structure in ZSM-5.[99] This structure was calculated employing the Fe_C model (Figure 6c). The two Fe atoms are calculated to be 2.634 Å from each other. The formal oxidation state of the two Fe atoms is 3. The spin state S = 8/2 was calculated to be the ground state and is more stable by 7.0 kcal·mol^{-1} than the state with S = 10/2. Therefore, the bis(μ-oxo)diiron structure in the studied *BEA zeolite was calculated to be an intermediate-spin species. There is no α oxygen like O atom in the structure and therefore the bridging O atoms could be responsible for the oxidative properties of the system.

The (μ-oxo)(μ-peroxo)diiron structure (Fe_D model; Figure 6d) was calculated to be the precursor of the (μ-oxo)diiron (Fe_E model; Figure 6e) species featuring two oxygen atoms forming double bonds to the two Fe atoms (the calculated bond lengths are 1.633 and 1.630 Å). These two O atoms resemble the α oxygen atom,[50,55,96,97] and they could be responsible for the oxidative properties of the system. The distances between the two Fe atoms were calculated to be equal to 3.234 and 3.432 Å for the Fe_D and Fe_E models, respectively. The calculations indicated that the ground state is connected with S = 8/2 for both the models. The formal oxidation state of the two Fe atoms is 4. These computational results indicate that these copper-oxo and iron-oxo species could exist in the investigated *BEA zeolite and lead to indications of their reactivity. The calculations of the relative stabilities (Table S1) also reveal that $[Fe(IV)(=O)O(=O)Fe(IV)]^{2+}$ (the Fe_E model) is more stable than $[Fe(IV)(O)O-OFe(IV)]^{2+}$ (the Fe_D model) and $[Fe(III)O_2Fe(III)]^{2+}$ (the Fe_C model) by 4 and 13 kcal/mol, respectively.

The mono(μ-oxo)dicopper and bis(μ-oxo)dicopper structures considered in this study were extensively investigated as species able to catalyze the oxidation of methane to methanol. Palagin et al.[94] studied $[CuOCu]^{2+}$ and $[Cu_xO_x]^{2+}$ (x = 2, 3, 4, and 5) in mordenite and showed that $[CuO_2Cu]^{2+}$ was calculated to be more stable in mordenite than $[CuOCu]^{2+}$, while the opposite is found for ZSM-5[95] and the Al-rich *BEA zeolite of this study (Table S1). Moreover, the *BEA zeolite lacks 8-rings; therefore, $[Cu_3O_3]^{2+}$ species formed in 8-rings of mordenite are not likely to be created in the *BEA zeolite. Kulkarni et al.[100] compared the ability of various $[M-O]^{1+,2+}$, $[M-OH]^{1+,2+}$, $[M-O-M]^{2+}$, $[M(\mu O)_2M]^{2+}$, $[M_3(\mu O)_3]^{2+}$, and $[Cu_6O_7]^{2+}$ motifs (transition-metal cations: Fe, Co, Ni, and Cu; zeolite topologies: AEI, AFX, CHA, MAZ, MOR, MFI, TON, FAU as well as binding sites in 6-, 8-, 10-, and 12-rings) to activate the C−H bond in the selective oxidation of methane to methanol. Arvidsson et al.[101] studied the direct conversion of methane into methanol over the $[M-O-M]^{2+}$ (M = Cu, Ni, Co, Fe, Ag, and Au) motif in the ZSM-5 structure and showed that the motif is a relevant candidate for the active site in ZSM-5 especially for Cu (the activity of $[M-O-M]^{2+}$ is calculated to be in the order of Cu > Ni > Co > Fe) cations, while Ag and Au are rather inactive. Sushkevich et al.[102] investigated the direct functionalization of methane to yield methanol over Cu-exchanged mordenite. They employed DFT calculations to show that the conversion of methane into methanol can be catalyzed by the $[Cu-O-Cu]^{2+}$ species in the 8-ring of mordenite.

Various iron-oxo species were considered to be responsible for the catalytic activity of iron-exchanged zeolites in the selective oxidation of methane by H_2O_2[103−106] and N_2O.[9,10,77,96,107−109] Hammond et al.[103−105] employed copper-promoted Fe-ZSM-5 to convert methane into methanol. They found that the $Fe_2[(\mu_2\text{-}OH)_2(OH)_2(H_2O)_2]^{2+}$ structure was the closest match between their EXAFS experiment and theoretical modeling. The authors concluded that this species corresponds to the resting state of the active site in ZSM-5. This structure is the protonated and hydrated analogue of the bis(μ-oxo)diiron species (Fe_C model). Pannov et al.[96] proposed the α oxygen created from N_2O, whose structure was determined by Snyder et al.[109] to selectively oxidize methane to methanol. The Fe_A, Fe_B, and Fe_E models (Figure 6a,b,e, respectively) possess oxygen atoms, which resemble the α oxygen atom, forming double bonds to Fe. However, the structure and relative stability of the investigated $[Cu_2O_y]^{2+}$ and $[Fe_2O_y]^{2+,3+}$ species in zeolites depend on the topology of the zeolite, the Al distribution, and Al siting in the framework of that zeolite forming various Al−Si_x−Al sequences balancing the positive charge of the $[M_xO_y]^{n+}$ species. Moreover, various computational methods (i.e., cluster model vs periodic DFT, various DFT functionals) were employed to study the $[M_xO_y]^{n+}$ species. These variabilities in terms of the zeolite topology, the Al siting, and the Al distribution and the computational method used make comparison of the results of these studies very difficult.

3.5. Structure and Nature of Cu and Fe Sites. *3.5.1. Cu Species in Al-Rich Cu-*BEA.* The UV−vis spectra of the air-activated Al-rich Cu-*BEA (Figure 2) were consistent with the prevailing presence of various isolated Cu^{2+} ions and a small number of dimeric Cu core species. The observed changes after exposure to methane at various temperatures confirmed the high reactivity of the dinuclear Cu^{2+} species and showed different redox behavior of the isolated Cu^{2+} ions depending on the local environment influenced by the charge of the zeolite framework. Bare Cu^{2+} ions coordinated exclusively to framework oxygens and balanced mostly by the charge from two Al atoms in the framework are highly stabilized and do not interact with methane molecules even at 500 °C. On the other hand, isolated Cu^{2+} ions partially charge-balanced by the charge from one aluminum atom are less stabilized and can be reduced in a methane atmosphere at intermediate temperatures of ∼400 °C. Dimeric Cu clusters with an active oxygen exhibited redox behavior, enabling a redox reaction with methane at much lower temperatures of ∼250 °C. The UV−vis absorption bands at 22 500 and 28 700 cm^{-1} are consistent with the presence of some (μ-oxo)dicopper (Cu_A model, Figure 5a) or bis(μ-oxo)dicopper (Cu_B model, Figure 5b), and the theoretical

https://dx.doi.org/10.1021/acscatal.9b05431
ACS Catal. 2020, 10, 3984−4002

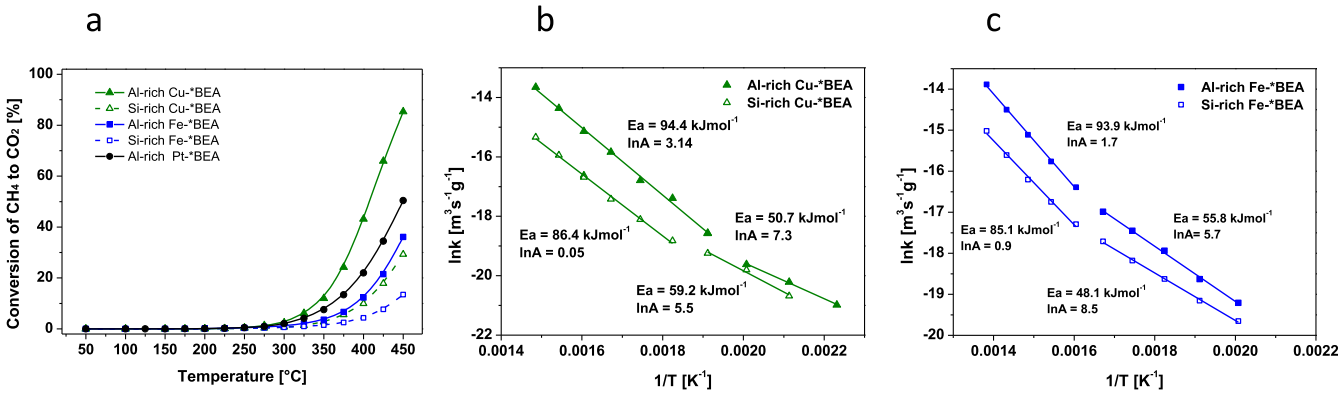

Figure 7. Oxidation of methane over Cu-, Fe-, and Pt-*BEA catalysts. (a) Conversion of methane into CO_2 and Arrhenius plots for (b) Cu and (c) Fe zeolites.

calculations confirmed that these species with active bridging O atoms could be formed in the Al-rich *BEA zeolite.

*3.5.2. Fe Species in Al-Rich Fe-*BEA.* The presence of intensive characteristic spectral bands of isolated Fe^{3+}-oxo in octahedral and tetrahedral coordinations, dimeric and oligomeric Fe-oxo moieties, and a very small intensity for bulk oxides in the complementary UV−vis (Figure 2) and Mössbauer (Figure 4) spectra indicated the heterogeneity of the Fe species in the Al-rich Fe-*BEA. The TPR-H_2 measurements and analysis of the absorption bands characteristic of isolated Fe^{3+}-oxo and dimeric/oligomeric Fe-oxo species after interaction with methane at various temperatures of 250−500 °C clearly showed that the redox properties are controlled by the structure, nuclearity, and coordination of the Fe^{3+} species in the zeolite. The tetrahedral coordination of isolated Fe^{3+}-oxo species to the oxygens in the zeolite framework stabilizes their redox state in a methane atmosphere even at high temperatures. Consequently, the tetrahedrally coordinated isolated Fe^{3+}-oxo species can hardly participate in a redox process with methane at <500 °C. Isolated octahedral Fe^{3+}-oxo species undergo redox transformation with methane with the participation of its oxygen ligand at ∼400 °C and could be involved in a redox catalytic reaction at intermediate temperatures. The reduction of the Fe^{3+} ions and interaction of the oxygen in the dimeric/oligomeric species with methane already occur at 250 °C. Theoretical calculations and the broad spectral features indicate the possible presence of a variety of μ-oxo, bis(μ-oxo), and (μ-oxo)(μ-peroxo)diiron species (Figure 6). The DFT model structures indicate the presence of oxygen-resembling "α-oxygen"-like atoms in the structures as well as reactive bridging O atoms potentially responsible for the oxidative properties of the system.

3.6. Activity of Cu- and Fe-*BEA Zeolites in Oxidation of Hydrocarbons. *3.6.1. Oxidation of Methane by Molecular Oxygen.* Conversion of methane into CO_2 in excess oxygen as a function of temperature over the Cu-, Fe-, and Pt -*BEA catalysts is shown in Figure 7a. The oxidation was selective for CO_2, whereas CH_3OH and CO were not detected in the products. The catalysts exhibited low conversions (≤1%) at very low temperatures of ∼200 °C; however, higher temperatures were needed for greater conversions (e.g., conversions of 43, 22, and 12% were observed at 400 °C for Al-rich Cu-, Pt-, and Fe-*BEA, respectively). A low reaction rate at temperatures of about 200−250 °C was also reported for the selective formation of methanol in a pseudocatalytic cyclic process in oxidation of a methane molecule by the activated oxygen bound in Cu active sites.[3] The significantly higher conversions obtained on Al-rich compared to those on Si-rich catalysts are consistent with the presence of a very large amount of the Cu- and Fe-ion species with versatile redox behavior, as observed in the UV−vis (Figures 2 and 3) and Mössbauer (Figure 4 and Table 3) spectra and TPR profiles (Figure 1) and shown in previous studies.[32,34,110] A very important finding is that Cu species in Al-rich *BEA zeolites can provide higher activity than the Pt-based catalyst.

The Arrhenius plots of methane oxidation over the Cu- and Fe-*BEA catalysts (Figure 7b,c) clearly showed two linear dependences with different slopes in the low- and high-temperature regions. The activation energies ranged from ca. 50 to 60 kJ mol^{-1} at 225−325 °C and from 80 to 90 kJ mol^{-1} at 350−450 °C. The activation energies correspond to a reaction step involving breaking of the strong C−H bond in the methane molecule, which is the rate-determining step.[11,17] Subsequent reactions of the activated molecule have much lower energy barriers and inexorably lead to the formation of H_2O and CO_2 from a desorbed partially oxidized intermediate in the presence of molecular oxygen. Two different activation energies for the low and high temperature can be attributed to the participation of different structures of the active sites in breaking the C−H bond. A stronger hydrogen affinity and lower activation barriers of C−H activation were reported for various dimeric Cu active sites compared to isolated Cu. The energy barriers for methane activation over the $[Cu-O-Cu]^{2+}$ entities in ZSM-5 (65 kJ mol^{-1})[11] and MOR (46 kJ and 61 kJ mol^{-1})[62] zeolites were obtained experimentally. However, the theoretical studies using density functional theory (DFT) calculations indicated that the various locations, coordinations, and hydroxylations of the $[Cu-O-Cu]^{2+}$ entities in the zeolitic channels could slightly alter the activation energy associated with methane oxidation.[111] The UV−vis spectra of the Al-rich Cu-*BEA zeolite (Figure 2) showed high reactivity of the dinuclear $[Cu_2(\mu\text{-}O)_2]^{2+}$ toward the interaction with a methane molecule. The low-temperature kinetic region is thus clearly associated with the oxidation of methane over the dinuclear Cu sites. This is also consistent with the similar observed activation energy for oxidation of CH_4 to CO_2 and the published activation energy for activation of the C−H bond over the dinuclear Cu sites.[11,62] The activation of the methane molecule proceeds via C−H bond cleavage and the subsequent rebound reaction mechanism, resulting in methanol and a reduced Cu cluster.[3] The reaction of the formed methanol with an oxygen atom from the reoxidated site or a nearby active center in the Al-rich Cu-*BEA leads to complete oxidation to CO_2 in excess oxygen even at low temperatures. The lower

https://dx.doi.org/10.1021/acscatal.9b05431
ACS Catal. 2020, 10, 3984−4002

Table 4. Complete Oxidation of Methane. Comparison of the Activities of Al-Rich Cu-*BEA and Reported Metal/Metal/Oxo Catalysts

catalyst	T_{10} (°C)	T_{50} (°C)	T_{90} (°C)	GHSV (h^{-1})	methane inlet (ppm)	ref
Al-rich Cu-*BEA	**340**	**407**	**455**	20 000	1000	this study
Supported and Oxidelike Cu Catalysts						
Cu−Mg−Al-oxide	442	527	568	VHSV 20 000	1 vol %	114
CuO/CeO_2	388	483	583	27 000	1 vol %	113
CuO/Cr_2O_3	400	525	630	14 000 mL/g h	1%	115
CuO/ZrO_2	410	490	568	30 000	1.4%	116
$CuO/MgAl_2O_4$	455	525	615	15 000−25 000	1 vol %	117
Cu−Ce−Mg−Al-oxide	376	442	520	16 000	1 vol %	
Cu(5%)Zn−Al-oxide	462	536	624	20 000	1 vol %	123
$LaSrCuO_4$		660		50 000 mL/g h	2%	120
Supported and Oxidelike Ce, Co, Fe, and Mn Catalysts						
$3\%Ce_{0.5}Tb_{0.5}O_x/MgO$	486	586	696	32 000 mL/g h	2.5%	121
meso-Co_3O_4/10%La-CeO_2	325	420	460	WHSV 180 000	1000	122
Ce(11%) Mg−Al-oxide	450	561	637	VHSV 16 000	1 vol %	123
$LaSrCuO_4$		660		50 000 mL/g h	2%	120
$La_{0.6}Sr_{0.4}MnO_3$	370	482	705	50 000	2 vol %	124
$La_{0.6}Sr_{0.4}MnO_3$	437	566	661	30 000	2%	125
$Ca(Mn_{0.6}Ti_{0.4})O_3$	467	585	664	30 000 mL/g h	3%	126
meso-LaCoO3	330	475	580	60 000	0.8%	127
$LaFeAl_{11}O_{19}$	450	555	640	48 000	1 vol %	128
$La_{1.9}Sr_{0.1}NiAlO_6$	379	501	603	48 000	2 vol %	129
$LaSrCuO_4$		660		50 000 mL/g h	2%	120
3DOM-m $La_{0.7}Ce_{0.3}CoO_3$		479	555	30 000 mL/g h	2 vol %	130
$NiO/LaNiO_3$	355	480	565	6000 mL/g h	6.7 vol %	131
$10Co/ZrO_2$		475	520	40 000	1 vol %	132
$7Fe_2O_3/Ce_{0.1}Co_{0.9}O_{1.1}$	390	490	560	32 000	2.5%	133
$15Mn/Al_2O_3$	453	467	510	40 000 mL/g h	20%	134
Pd, Pt, and Au Catalysts						
0.1 Pd/H-*BEA Si/Al_2 738	287	359	402	335 000	2000	135
1 Pd/Na-MOR		335	375	70 000	1 vol %	136
1 Pd/SSZ-13 Si/Al 52	230	311	375	13 600	0.05 vol %	137
0.1 Pd/H-ZSM-5 Si/Al_2=1100	297	377	407	335 000	2000	135
1 Pd/ZSM-5	277	335	374	36 000	2000	138
2 Pd/Al_2O_3	270	325	370	15 000	1 vol %	139
2 Pd/TiO_2-Al_2O_3	300	352	395	33 000 mL/h g	1%	140
$1Pt/Cr_2O_3$	320	350	395	30 000 mL/h g	0.2 vol %	141
$2Au\text{-}2Pt/Co_3O_4$		295	332	10 000	1 vol %	142
Au/Co_3O_4	270	364	450	WHSV 60 000	0.3 vol %	143

activation energy and the interaction of methane with the dimeric μ-oxo Cu sites in the low-temperature region and the higher activation energy and the interaction of methane with isolated divalent copper cations in the cationic zeolite positions in the high-temperature region are consistent with low- and high-temperature mechanisms over dimeric Cu^{2+} and isolated Cu^{2+}, respectively. The higher pre-exponential factors obtained from the Arrhenius plots for the Al-rich Cu-*BEA compared to those of the Si-rich Cu-*BEA sample are consistent with higher concentrations of the active sites.

The activity of Al-rich Fe-*BEA was significantly lower compared to that of the Al-rich Cu-*BEA. It was well documented in the literature that well-dispersed Fe^{2+} ions in Fe-ZSM-5[9,10] and Fe-CHA[112] can form after interaction with N_2O an active oxygen capable of oxidizing methane at ambient temperatures. The interaction of N_2O and Fe^{2+} ions mostly compensated by the charge from framework Al pairs[112] yields α-O atomic oxygen, which is capable of breaking a strong C−H bond at close to room temperature. For the molecular oxygen used as an oxidant in this study, both the UV−vis and Mössbauer spectra, along with the performed calculations, suggest that the most reactive oxygen species may be formed on the iron dimers/oligomers. Unlike the atomic oxygen that is formed from N_2O, these activated oxygen atoms are capable of the activation and complete oxidation of methane at much higher temperatures.

Conventional methane oxidation catalysts are based on mixed oxides or on precious metals, in particular palladium. Table 4 compares the activities of the most active Al-rich Cu-*BEA with supported and oxidelike Cu catalysts, Ce-, Co-, Fe-, and Mn-based catalysts of various structures and compositions, and supported Pd catalysts found in the literature. The T_{50} value for the Al-rich Cu-*BEA is 407 °C, while for the supported and mixed Cu-oxo catalyst, it is typically in the 450−550 °C[113−120] range. The supported and mixed Cu-oxo catalysts generally exhibit lower activity than the Al-rich Cu-*BEA. For comparison, the data reported for Ce, Co, Fe, and Mn catalysts optimized and designed for total oxidation of methane are also included (Table 4). The coordination and the arrangement of the Cu ions in the Al-rich *BEA zeolites provide significantly higher activity compared to most conventional supported or

https://dx.doi.org/10.1021/acscatal.9b05431
ACS Catal. 2020, 10, 3984−4002

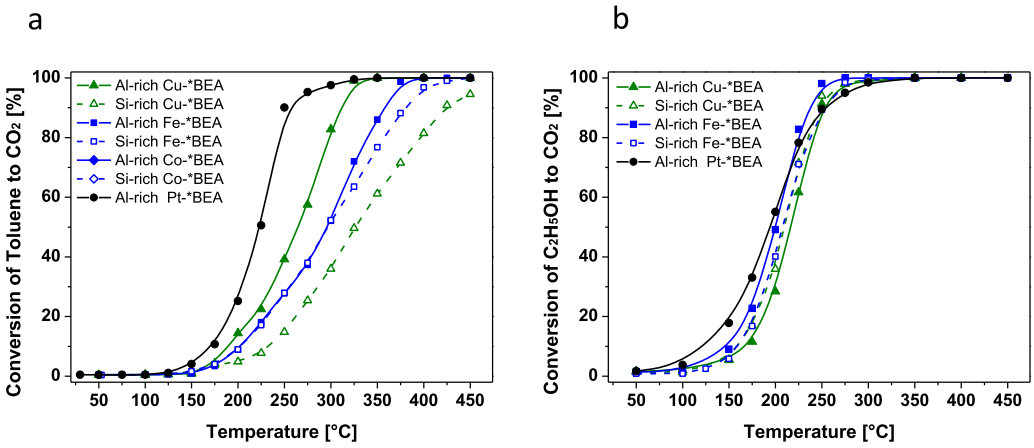

Figure 8. Oxidation of (a) toluene and (b) ethanol over Cu-, Fe-, and Pt-*BEA catalysts as a function of temperature.

Table 5. Complete Oxidation of Toluene. Comparison of the Activities of Al-Rich Cu- and Fe-*BEA and Reported Metal/Metal/Oxo Catalysts

catalyst	T_{50} (°C)	T_{98} (°C)	GHSV (h^{-1})	toluene inlet (ppm)	ref
Al-rich Cu-*BEA	**264**	**325**	20 000	200	this study
Al-rich Fe-*BEA	**295**	**376**	20 000	200	
Supported and Oxidelike Cu and Fe Catalysts					
7Fe/SBA-15	313	404	20 000 mL/g h	1000	144
5Cu/Fe_2O_3+Na-X	292		30 000 mL/g h		145
Fe/montmorillonite	285	380	36 000		146
9.5Fe_2O_3/clinoptilolite	333	not reached	15 000	1000	147
41.6Fe/pillared montmorillonite	202	375	~6000	4000	148
9.5CuO/HCLT	330	545	15 000	1000	147
20Cu/H(halloysite)	320	385			149
9Cu/SBA-15	312	432	WHSV of 1.2 h^{-1}		150
9Cu/SBA-16	337	442	WHSV of 1.2 h^{-1}		150
Supported and Oxidelike Ce, Co, and Mn Catalysts					
$LaCoO_3$	244	395		1700	158
La0.7Sr0.3Co0.8Fe0.2O_3 (+ 5% Co)	203	280	15 000 mL/g h	500	159
$MnFe_2O_4$	282		60 000 mL/g h	1700	160
Co/Mg−Al(hydrotalcite)	320	355	20 000 mL/g h	2700	161
MnCuAl hydrotalcite	258	298	75 000 mL/g h	800	162
$MgAlMnO_4$	264	340	30 000	430	163
CoAl hydrotalcite	271	277	60 000 mL/g h	1000	164
Mn_3O_4	225	265	19 100	1000	165
Co_3O_4-MnO_x (Mn:Co = 1:2)	225	245	30 000 mL/g h	1000	166
20Ce/alumina	265	290	54 000 mL/g h	1400	167
9.5MnO_2/α-Al_2O_3	213	332	15 000	1000	168
Fe-Mn/cordierite	180	400	10 000	1000	169
Pt Catalysts					
1Pt/*BEA	186	195	60 000	1000	152
1Pt/KBeta-SDS	142	150	60 000	1000	153
1Pt/KBeta-TEA	157	160	60 000	1000	153
0.5Pt/Meso-KZSM-5	172	175	60 000	1000	154
0.5Pt/KZSM-5-100 (Si/Al 100)	162	169	60 000	1000	155
1Pt/HPMOR	175	200	60 000	1000	156

mixed catalysts.[121−134] This emphasizes the unique activity of the Cu sites coordinated in the Al-rich *BEA zeolites. To confirm the stability of the catalytic activity of the Al-rich Cu-*BEA zeolite, the conversion and selectivity of methane oxidation were analyzed as a function of time on stream. The methane conversion and also the complete selectivity for CO_2 were stable at 420 °C in time on stream of 24 h. Comparisons of the published values of T_{10}, T_{50}, and T_{90} for precious metal catalysts (Table 4),[135−143] especially palladium catalysts, and those obtained for the Al-rich Cu-*BEA zeolite show that a temperature of about 50 °C higher has to be used when using the zeolite catalyst to achieve similar conversions

3.6.2. Activity in the Total Oxidation of Toluene and Ethanol. Toluene and ethanol were used as model compounds representing aromatic and oxygenated VOCs, respectively. Figure 8a shows the conversion of toluene into CO_2 as a

https://dx.doi.org/10.1021/acscatal.9b05431
ACS Catal. 2020, 10, 3984−4002

Table 6. Complete Oxidation of Ethanol. Comparison of the Activities of Al-Rich Cu- and Fe-*BEA and Reported Metal/Metal/Oxo Catalysts

catalyst	T_{50} (°C)	T_{98} (°C)	GHSV (h^{-1})	ethanol inlet (ppm)	ref
Al-rich Fe-*BEA	**201**	**253**	20 000	250	this study
Al-rich Cu-*BEA	**216**	**281**	20 000	250	this study
0.5Pt/BEA	101	132	30 000 mL/g h	1000	157
0.34Pt/MOR	80	126	30 000 mL/g h	1000	157
MnCu mixed oxide	180	204	20 000 mL/g h	1%	170
$CuO-CeO_2$	210	225	50 000	1600	171
$Cu-Mn/Al_2O_3$	188	223	20 000	800	172
$LaFe_{0.9}Ni_{0.1}O_3$	247	282	60 000 mL/g h	1%	173
Mn_5O_8	205	238	53 050	930	174

function of the reaction temperature over Al-rich Cu- and Fe-*BEA catalysts and for comparison over Al-rich Pt-*BEA and Si-rich Cu- and Fe-*BEA zeolites. The temperatures for 50 and 90% conversions are given in Table 2. With the Al-rich Cu-*BEA catalyst, the conversion first started to increase at a temperature of approximately 150 °C and reached complete conversion at approximately 350 °C. The high activity of Al-rich Cu-*BEA facilitated a shift in the operational temperature window by ca. 60 °C compared to the Si-rich Cu-*BEA analogue. The reaction of toluene in an excess of molecular oxygen over the Al-rich Cu-*BEA zeolite was CO_2-selective without observation of any byproduct within the sensitivity of the measurement (>0.1 ppm). The Al-rich Fe-*BEA zeolite exhibited slightly lower activity compared to the Cu zeolite, as reflected in the T_{50} values of 295 and 264 °C for the Fe and Cu zeolite, respectively. At low temperatures, detectable concentrations of benzene (≤1 ppm) were observed in the reaction product over the Fe zeolites. This indicates that the active oxygen in the Fe sites primarily attacks the methyl group in the toluene molecule. Other byproducts were not observed and the reaction was CO_2-selective at higher temperatures of ≥275 °C. The values of T_{50} and T_{98} conversion for Al-rich Cu-*BEA indicate higher catalytic activity compared to most Fe and Cu oxides supported on silicalike materials (SBA-15, SBA-16) or aluminosilicates (montmorillonite, clinoptilolite, halloysite) (Table 5).[144−150] While the Al-rich Cu-*BEA catalyst was more active than platinum in the oxidation of methane, the reaction rates for Al-rich Cu-*BEA in the toluene oxidation were approximately 2 times lower compared to those for the platinum-based Al-rich Pt-*BEA catalyst. The different order of the activities is most probably due to the different mechanisms of the oxidation of toluene proceeding via a surface dissociative adsorption of oxygen on Pt as the rate-determining step.[151] In contrast, the C−H bond activation is a rate-determining step in the methane oxidation proceeding via a homolytic C−H bond cleavage facilitated by the interaction with a formally radical-anionic extraframework oxygen.[3] Platinum-based catalysts can yield a comparable conversion to that of a zeolite at a temperature about 100 °C lower (Table 5).[152−157] Comparisons with selected catalysts based on various transition metals show that, in particular, cobalt- and manganese-based catalysts can also provide slightly higher activity than Al-rich Cu- and Fe-*BEA catalysts (Table 5).[158−169]

Figure 8b shows the total oxidation of ethanol over the Cu-, Fe-, and Pt-*BEA samples, and Table 2 summarizes the obtained results. The dependence of the conversion as a function of temperature shows that temperatures for the oxidation of ethanol to CO_2 are about 200 °C lower than for methane. The much lower temperatures for total oxidation of ethanol compared to those for methane are a result of the lower strength of the H−C bonds, much higher polarity/basicity, and adsorption energy of ethanol compared to those of the tetrahedrally coordinated methane molecule with four equivalent strong C−H bonds. Comparison of the values for T_{50} and T_{98} for the Fe- and Cu-*BEA zeolites and a variety of Cu, Mn, Fe, and Pt catalysts (Table 6) shows that the reactive ethanol molecule can be oxidized by both activated oxygen at Cu and Fe sites in the zeolite but even more effectively by an active oxygen on the metal oxides[170−174] or dissociated oxygen at platinum.

The result clearly demonstrated that Fe and Cu sites stabilized in the matrix of *BEA catalysts in an oxygen-containing atmosphere generate active oxygens capable of total oxidation of toluene and ethanol as a typical model aromatic and alcohol, respectively. The advantage of the Al-rich Fe- and Cu-*BEA catalysts is that the oxidation of intermediate products is practically barrierless compared to the activation of the original reactant molecules and therefore CO_2-selective. Among reported catalysts for total oxidation of toluene, the activities of the Al-rich Fe- and Cu-*BEA are comparable with those of the most active p-type Mn, Fe, and Cu metal oxides with optimized structures.[175−177] The Al-rich Fe- and Cu-*BEA catalysts are unique in the oxidation of molecules with strong C−H bonds such as methane or toluene, while the highly reactive ethanol molecule can be more readily oxidized on many conventional oxide catalysts.

4. CONCLUSIONS

This study demonstrated the following characteristic features of the oxidation of methane, toluene, and ethanol by molecular oxygen over Cu- and Fe-*BEA zeolite catalysts:

(1) Three groups of Cu sites differing in their local coordination, nuclearity, and activity in the oxidation reactions are present in the Al-rich Cu-*BEA zeolite: (i) Dimeric Cu sites in the form of the (μ-oxo)dicopper or bis(μ-oxo)dicopper with active bridging O atoms, which enable oxidation of methane at low temperatures of ∼250 °C, (ii) isolated Cu^{2+} ions partially charge-balanced by the framework, which catalyze the oxidation of methane at higher temperatures of ≥350 °C, and (iii) highly stabilized bare Cu^{2+} ions coordinated exclusively to framework oxygens and balanced by the charge of the framework, which do not contribute to the activity.

(2) The redox properties and activity of Fe species in Al-rich Fe-*BEA are governed by their structure, nuclearity, and coordination. Active oxygen atoms in the dimeric/oligomeric species with a variety of possible μ-oxo, bis(μ-oxo), and (μ-oxo)(μ-peroxo) structures are responsible for the oxidation of methane in the low-temperature

https://dx.doi.org/10.1021/acscatal.9b05431
ACS Catal. 2020, 10, 3984−4002

region. Isolated Fe^{3+}-oxo ions in the octahedral coordination contribute to the oxidation reactions at higher temperatures of ≥350 °C, whereas isolated Fe^{3+}-oxo tetrahedrally coordinated to the framework oxygen does not exhibit redox properties in the methane oxidation.

(3) The Fe and Cu ionic species with a versatile redox state in the Al-rich *BEA zeolite effectively catalyze the oxidation of methane, toluene, and ethanol. The oxidation is nonspecific with a barrierless reaction of intermediate products and fully CO_2-selective in an excess of oxygen. The coordination and the unique arrangement of the Cu and Fe ions in the dinuclear sites with the active bridging oxygen and active isolated sites exhibit higher activity in the oxidation of hydrocarbon molecules with strong C−H bonds like methane and toluene compared to those of supported and mixed metal/metal-oxo catalysts.

■ ASSOCIATED CONTENT

Supporting Information

The Supporting Information is available free of charge at https://pubs.acs.org/doi/10.1021/acscatal.9b05431.

HR-TEM of the Al-rich Pt-*BEA zeolite, comparison of the relative stabilities of the computational models, and the Cartesian coordinates of the Cu and Fe structures (PDF)

■ AUTHOR INFORMATION

Corresponding Author

Petr Sazama − *Heyrovský Institute of Physical Chemistry, Academy of Sciences of the Czech Republic 182 23 Prague, Czech Republic;* orcid.org/0000-0001-7795-2681; Email: petr.sazama@jh-inst.cas.cz

Authors

Jaroslava Moravkova − *Heyrovský Institute of Physical Chemistry, Academy of Sciences of the Czech Republic 182 23 Prague, Czech Republic*

Stepan Sklenak − *Heyrovský Institute of Physical Chemistry, Academy of Sciences of the Czech Republic 182 23 Prague, Czech Republic;* orcid.org/0000-0003-4862-857X

Alena Vondrova − *Heyrovský Institute of Physical Chemistry, Academy of Sciences of the Czech Republic 182 23 Prague, Czech Republic*

Edyta Tabor − *Heyrovský Institute of Physical Chemistry, Academy of Sciences of the Czech Republic 182 23 Prague, Czech Republic;* orcid.org/0000-0002-4071-8610

Galina Sadovska − *Heyrovský Institute of Physical Chemistry, Academy of Sciences of the Czech Republic 182 23 Prague, Czech Republic*

Radim Pilar − *Heyrovský Institute of Physical Chemistry, Academy of Sciences of the Czech Republic 182 23 Prague, Czech Republic*

Complete contact information is available at: https://pubs.acs.org/10.1021/acscatal.9b05431

Notes

The authors declare no competing financial interest.

■ ACKNOWLEDGMENTS

This work was supported by the Grant Agency of the Czech Republic under Project No. 18-20303S. The authors acknowledge the assistance provided by the Research Infrastructures NanoEnviCz (Project No. LM2015073) and Pro-NanoEnviCz (Project No. CZ.02.1.01/0.0/0.0/16_013/0001821), supported by the Ministry of Education, Youth and Sports of the Czech Republic. The DFT calculations were supported by The Ministry of Education, Youth and Sports from the Large Infrastructures for Research, Experimental Development and Innovations project, "IT4Innovations National Science Center − LM2015070".

■ REFERENCES

(1) Groothaert, M. H.; Smeets, P. J.; Sels, B. F.; Jacobs, P. A.; Schoonheydt, R. A. Selective Oxidation of Methane by the Bis(μ-oxo)dicopper Core Stabilized on ZSM-5 and Mordenite Zeolites. *J. Am. Chem. Soc.* **2005**, *127*, 1394−1395.

(2) Groothaert, M. H.; van Bokhoven, J. A.; Battiston, A. A.; Weckhuysen, B. M.; Schoonheydt, R. A. Bis(μ-oxo)dicopper in Cu-ZSM-5 and Its Role in the Decomposition of NO: A Combined in Situ XAFS, UV−Vis−Near-IR, and Kinetic Study. *J. Am. Chem. Soc.* **2003**, *125*, 7629−7640.

(3) Grundner, S.; Markovits, M. A. C.; Li, G.; Tromp, M.; Pidko, E. A.; Hensen, E. J. M.; Jentys, A.; Sanchez-Sanchez, M.; Lercher, J. A. Single-site trinuclear copper oxygen clusters in mordenite for selective conversion of methane to methanol. *Nat. Commun.* **2015**, *6*, No. 7546.

(4) Ipek, B.; Wulfers, M. J.; Kim, H.; Göltl, F.; Hermans, I.; Smith, J. P.; Booksh, K. S.; Brown, C. M.; Lobo, R. F. Formation of $[Cu_2O_2]^{2+}$ and $[Cu_2O]^{2+}$ toward C−H Bond Activation in Cu-SSZ-13 and Cu-SSZ-39. *ACS Catal.* **2017**, *7*, 4291−4303.

(5) Le, H. V.; Parishan, S.; Sagaltchik, A.; Göbel, C.; Schlesiger, C.; Malzer, W.; Trunschke, A.; Schomäcker, R.; Thomas, A. Solid-State Ion-Exchanged Cu/Mordenite Catalysts for the Direct Conversion of Methane to Methanol. *ACS Catal.* **2017**, *7*, 1403−1412.

(6) Mahyuddin, M. H.; Staykov, A.; Shiota, Y.; Miyanishi, M.; Yoshizawa, K. Roles of Zeolite Confinement and Cu−O−Cu Angle on the Direct Conversion of Methane to Methanol by $[Cu_2(\mu\text{-}O)]^{2+}$-Exchanged AEI, CHA, AFX, and MFI Zeolites. *ACS Catal.* **2017**, *7*, 3741−3751.

(7) Schwach, P.; Pan, X.; Bao, X. Direct Conversion of Methane to Value-Added Chemicals over Heterogeneous Catalysts: Challenges and Prospects. *Chem. Rev.* **2017**, *117*, 8497−8520.

(8) Mahyuddin, M. H.; Shiota, Y.; Yoshizawa, K. Methane selective oxidation to methanol by metal-exchanged zeolites: a review of active sites and their reactivity. *Catal. Sci. Technol.* **2019**, *9*, 1744−1768.

(9) Dubkov, K. A.; Sobolev, V. I.; Talsi, E. P.; Rodkin, M. A.; Watkins, N. H.; Shteinman, A. A.; Panov, G. I. Kinetic isotope effects and mechanism of biomimetic oxidation of methane and benzene on FeZSM-5 zeolite. *J. Mol. Catal. A: Chem.* **1997**, *123*, 155−161.

(10) Panov, G. I.; Sobolev, V. I.; Dubkov, K. A.; Parmon, V. N.; Ovanesyan, N. S.; Shilov, A. E.; Shteinman, A. A. Iron complexes in zeolites as a new model of methane monooxygenase. *React. Kinet. Catal. Lett.* **1997**, *61*, 251−258.

(11) Woertink, J. S.; Smeets, P. J.; Groothaert, M. H.; Vance, M. A.; Sels, B. F.; Schoonheydt, R. A.; Solomon, E. I. A. $[Cu_2O]^{2+}$ core in Cu-ZSM-5, the active site in the oxidation of methane to methanol. *Proc. Natl. Acad. Sci. U.S.A.* **2009**, *106*, 18908.

(12) Pappas, D. K.; Martini, A.; Dyballa, M.; Kvande, K.; Teketel, S.; Lomachenko, K. A.; Baran, R.; Glatzel, P.; Arstad, B.; Berlier, G.; Lamberti, C.; Bordiga, S.; Olsbye, U.; Svelle, S.; Beato, P.; Borfecchia, E. The Nuclearity of the Active Site for Methane to Methanol Conversion in Cu-Mordenite: A Quantitative Assessment. *J. Am. Chem. Soc.* **2018**, *140*, 15270−15278.

(13) Mahyuddin, M. H.; Tanaka, T.; Staykov, A.; Shiota, Y.; Yoshizawa, K. Dioxygen Activation on Cu-MOR Zeolite: Theoretical Insights into the Formation of Cu_2O and Cu_3O_3 Active Species. *Inorg. Chem.* **2018**, *57*, 10146−10152.

(14) Smeets, P. J.; Groothaert, M. H.; Schoonheydt, R. A. Cu based zeolites: A UV−vis study of the active site in the selective methane oxidation at low temperatures. *Catal. Today* **2005**, *110*, 303−309.

(15) Smeets, P. J.; Groothaert, M. H.; van Teeffelen, R. M.; Leeman, H.; Hensen, E. J. M.; Schoonheydt, R. A. Direct NO and N_2O decomposition and NO-assisted N_2O decomposition over Cu-zeolites: Elucidating the influence of the CuCu distance on oxygen migration. *J. Catal.* **2007**, *245*, 358−368.
(16) Groothaert, M. H.; Lievens, K.; Leeman, H.; Weckhuysen, B. M.; Schoonheydt, R. A. An operando optical fiber UV−vis spectroscopic study of the catalytic decomposition of NO and N_2O over Cu-ZSM-5. *J. Catal.* **2003**, *220*, 500−512.
(17) Dinh, K. T.; Sullivan, M. M.; Narsimhan, K.; Serna, P.; Meyer, R. J.; Dincă, M.; Román-Leshkov, Y. Continuous Partial Oxidation of Methane to Methanol Catalyzed by Diffusion-Paired Copper Dimers in Copper-Exchanged Zeolites. *J. Am. Chem. Soc.* **2019**, *141*, 11641−11650.
(18) Shteinman, A. A. The mechanism of methane and dioxygen activation in the catalytic cycle of methane monooxygenase. *FEBS Lett.* **1995**, *362*, 5−9.
(19) Tinberg, C. E.; Lippard, S. J. Dioxygen activation in soluble methane monooxygenase. *Acc. Chem. Res.* **2011**, *44*, 280−288.
(20) Lee, S. J. Hydroxylation of methane through component interactions in soluble methane monooxygenases. *J. Microbiol.* **2016**, *54*, 277−282.
(21) Dinh, K. T.; Sullivan, M. M.; Serna, P.; Meyer, R. J.; Dincă, M.; Román-Leshkov, Y. Viewpoint on the Partial Oxidation of Methane to Methanol Using Cu- and Fe-Exchanged Zeolites. *ACS Catal.* **2018**, *8*, 8306−8313.
(22) Myronova, N.; Kitmitto, A.; Collins, R. F.; Miyaji, A.; Dalton, H. Three-dimensional structure determination of a protein supercomplex that oxidizes methane to formaldehyde in Methylococcus capsulatus (Bath). *Biochemistry* **2006**, *45*, 11905−11914.
(23) Narsimhan, K.; Iyoki, K.; Dinh, K.; Román-Leshkov, Y. Catalytic Oxidation of Methane into Methanol over Copper-Exchanged Zeolites with Oxygen at Low Temperature. *ACS Cent. Sci.* **2016**, *2*, 424−429.
(24) Yamamoto, S. Latest research and development of gas occlusion materials. Automotive exhaust gas purifying catalyst using zeolite adsorber: Outline of hydrocarbon-adsorption type three-way catalyst. *Petrotech* **2003**, *26*, 119−124.
(25) Moden, B.; Donohue, J. M.; Cormier, W. E.; Li, H. X. The uses and challenges of zeolites in automotive applications. *Top. Catal.* **2010**, *53*, 1367−1373.
(26) Kobatake, Y.; Momma, K.; Elangovan, S. P.; Itabashi, K.; Okubo, T.; Ogura, M. "Super Hydrocarbon Reformer Trap" for the Complete Oxidation of Toluene Using Iron-Exchanged β-Zeolite with a Low Silicon/Aluminum Ratio. *ChemCatChem* **2016**, *8*, 2516−2524.
(27) Petrov, A. W.; Ferri, D.; Kröcher, O.; van Bokhoven, J. A. Design of Stable Palladium-Based Zeolite Catalysts for Complete Methane Oxidation by Postsynthesis Zeolite Modification. *ACS Catal.* **2019**, *9*, 2303−2312.
(28) Petrov, A. W.; Ferri, D.; Krumeich, F.; Nachtegaal, M.; van Bokhoven, J. A.; Kröcher, O. Stable complete methane oxidation over palladium based zeolite catalysts. *Nat. Commun.* **2018**, *9*, No. 2545.
(29) Gélin, P.; Primet, M. Complete Oxidation of Methane at Low Temperature Over Noble Metal Based Catalysts: A Review. *Appl. Catal., B* **2002**, *39*, 1−37.
(30) Allen, G. Rebalancing the global methane budget. *Nature* **2016**, *538*, 46.
(31) Schwietzke, S.; Sherwood, O. A.; Bruhwiler, L. M. P.; Miller, J. B.; Etiope, G.; Dlugokencky, E. J.; Michel, S. E.; Arling, V. A.; Vaughn, B. H.; White, J. W. C.; Tans, P. P. Upward revision of global fossil fuel methane emissions based on isotope database. *Nature* **2016**, *538*, 88.
(32) Sazama, P.; Pilar, R.; Mokrzycki, L.; Vondrova, A.; Kaucky, D.; Plsek, J.; Sklenak, S.; Stastny, P.; Klein, P. Remarkably enhanced density and specific activity of active sites in Al-rich Cu-, Fe- and Co-beta zeolites for selective catalytic reduction of NO_x. *Appl. Catal., B* **2016**, *189*, 65−74.
(33) Sazama, P.; Tabor, E.; Klein, P.; Wichterlova, B.; Sklenak, S.; Mokrzycki, L.; Pashkkova, V.; Ogura, M.; Dedecek, J. Al-rich beta zeolites. Distribution of Al atoms in the framework and related protonic and metal-ion species. *J. Catal.* **2016**, *333*, 102−114.
(34) Sazama, P.; Wichterlová, B.; Sklenák, Š.; Parvulescu, V. I.; Candu, N.; Sádovská, G.; Dědeček, J.; Klein, P.; Pashkova, V.; Šťastný, P. Acid and redox activity of template-free Al-rich H-BEA* and Fe-BEA* zeolites. *J. Catal.* **2014**, *318*, 22−33.
(35) Sazama, P.; Kaucky, D.; Moravkova, J.; Pilar, R.; Klein, P.; Pastvova, J.; Tabor, E.; Sklenak, S.; Jakubec, I.; Mokrzycki, L. Superior activity of non-interacting close acidic protons in Al-rich Pt/H-*BEA zeolite in isomerization of n-hexane. *Appl. Catal., A* **2017**, *533*, 28−37.
(36) Wichterlová, B.; Sobalík, Z.; Skokánek, M. Effect of water vapour and ammonia on the solid-solid interaction of Cu oxide with Y-type zeolite: preparation of catalyst for reduction of nitric oxide with ammonia at low temperature. *Appl. Catal., A* **1993**, *103*, 269−280.
(37) Kresse, G.; Hafner, J. Ab-Initio Molecular-Dynamics for Open-Shell Transition-Metals. *Phys. Rev. B* **1993**, *48*, 13115−13118.
(38) Kresse, G.; Hafner, J.; Kresse, G.; Hafner, J. Ab-Initio Molecular-Dynamics Simulation of the Liquid-Metal Amorphous-Semiconductor Transition in Germanium. *Phys. Rev. B* **1994**, *49*, 14251−14269.
(39) Kresse, G.; Furthmuller, J. Efficient iterative schemes for ab initio total-energy calculations using a plane-wave basis set. *Phys. Rev. B* **1996**, *54*, 11169−11186.
(40) Kresse, G.; Furthmuller, J. Efficiency of ab-initio total energy calculations for metals and semiconductors using a plane-wave basis set. *Comput. Mater. Sci.* **1996**, *6*, 15−50.
(41) Blöchl, P. E. Projector Augmented-Wave Method. *Phys. Rev. B* **1994**, *50*, 17953−17979.
(42) Kresse, G.; Joubert, D. From ultrasoft pseudopotentials to the projector augmented-wave method. *Phys. Rev. B* **1999**, *59*, 1758−1775.
(43) Perdew, J. P.; Burke, K.; Ernzerhof, M. Generalized gradient approximation made simple. *Phys. Rev. Lett.* **1996**, *77*, 3865−3868.
(44) Steinmann, S. N.; Corminboeuf, C. Comprehensive Bench marking of a Density-Dependent Dispersion Correction. *J. Chem. Theory Comput.* **2011**, *7*, 3567−3577.
(45) Steinmann, S. N.; Corminboeuf, C. A generalized-gradient approximation exchange hole model for dispersion coefficients. *J. Chem. Phys.* **2011**, *134*, No. 044117.
(46) Grimme, S. Accurate description of van der Waals complexes by density functional theory including empirical corrections. *J. Comput. Chem.* **2004**, *25*, 1463−1473.
(47) Nosé, S. A Unified Formulation of the Constant Temperature Molecular-Dynamics Metods. *J. Chem. Phys.* **1984**, *81*, 511−519.
(48) Verlet, L. Computer Experiments on Classical Fluids. I. Thermodynamical Properties of Lennard-Jones Molecules. *Phys. Rev.* **1967**, *159*, 98−103.
(49) Verlet, L. Computer Experiments on Classical Fluids. II. Equilibrium Correlation Functions. *Phys. Rev.* **1968**, *165*, 201−214.
(50) Sklenak, S.; Andrikopoulos, P. C.; Boekfa, B.; Jansang, B.; Novakova, J.; Benco, L.; Bucko, T.; Hafner, J.; Dedecek, J.; Sobalik, Z. N_2O decomposition over Fe-zeolites: Structure of the active sites and the origin of the distinct reactivity of Fe-ferrierite, Fe-ZSM-5, and Fe-beta. A combined periodic DFT and multispectral study. *J. Catal.* **2010**, *272*, 262−274.
(51) Sklenak, S.; Andrikopoulos, P. C.; Whittleton, S. R.; Jirglova, H.; Sazama, P.; Benco, L.; Bucko, T.; Hafner, J.; Sobalik, Z. Effect of the Al Siting on the Structure of Co(II) and Cu(II) Cationic Sites in Ferrierite. A Periodic DFT Molecular Dynamics and FTIR Study. *J. Phys. Chem. C* **2013**, *117*, 3958−3968.
(52) Klein, P.; Dedecek, J.; Thomas, H. M.; Whittleton, S. R.; Pashkova, V.; Brus, J.; Kobera, L.; Sklenak, S. NMR crystallography of monovalent cations in inorganic matrixes: Li^+ siting and the local structure of Li^+ sites in ferrierites. *Chem. Commun.* **2015**, *51*, 8962−8965.
(53) Karcz, R.; Dedecek, J.; Supronowicz, B.; Thomas, H. M.; Klein, P.; Tabor, E.; Sazama, P.; Pashkova, V.; Sklenak, S. TNU-9 Zeolite: Aluminum Distribution and Extra-Framework Sites of Divalent Cations. *Chem. − Eur. J.* **2017**, *23*, 8857−8870.
(54) Mlekodaj, K.; Dedecek, J.; Pashkova, V.; Tabor, E.; Klein, P.; Urbanova, M.; Karcz, R.; Sazama, P.; Whittleton, S. R.; Thomas, H. M.; Fishchuk, A. V.; Sklenak, S. Al Organization in the SSZ-13 Zeolite. Al

Distribution and Extraframework Sites of Divalent Cations. *J. Phys. Chem. C* **2019**, *123*, 7968−7987.
(55) Tabor, E.; Lemishka, M.; Sobalik, Z.; Mlekodaj, K.; Andrikopoulos, P. C.; Dedecek, J.; Sklenak, S. Low-temperature selective oxidation of methane over distant binuclear cationic centers in zeolites. *Commun. Chem.* **2019**, *2*, No. 71.
(56) Civiš, S.; Babánková, D.; Cihelka, J.; Sazama, P.; Juha, L. Spectroscopic investigations of high-power laser-induced dielectric breakdown in gas mixtures containing carbon monoxide. *J. Phys. Chem. A* **2008**, *112*, 7162−7169.
(57) Sazama, P.; Wichterlová, B.; Tábor, E.; Šťastný, P.; Sathu, N. K.; Sobalík, Z.; Dědeček, J.; Sklenák, Š.; Klein, P.; Vondrová, A. Tailoring of the structure of Fe-cationic species in Fe-ZSM-5 by distribution of Al atoms in the framework for N_2O decomposition and NH_3-SCR-NO_x. *J. Catal.* **2014**, *312*, 123−138.
(58) Sazama, P.; Sathu, N. K.; Tabor, E.; Wichterlová, B.; Sklenák, Š.; Sobalík, Z. Structure and critical function of Fe and acid sites in Fe-ZSM-5 in propane oxidative dehydrogenation with N_2O and N_2O decomposition. *J. Catal.* **2013**, *299*, 188−203.
(59) Wichterlová, B.; Sobalík, Z.; Skokánek, M. Effect of water vapour and ammonia on the solid-solid interaction of Cu oxide with Y-type zeolite: preparation of catalyst for reduction of nitric oxide with ammonia at low temperature. *Appl. Catal., A* **1993**, *103*, 269−280.
(60) Kefirov, R.; Penkova, A.; Hadjiivanov, K.; Dzwigaj, S.; Che, M. Stabilization of Cu^+ ions in BEA zeolite: Study by FTIR spectroscopy of adsorbed CO and TPR. *Microporous Mesoporous Mater.* **2008**, *116*, 180−187.
(61) Szegedi, Á.; Kónya, Z.; Méhn, D.; Solymár, E.; Pál-Borbély, G.; Horváth, Z. E.; Biró, L. P.; Kiricsi, I. Spherical mesoporous MCM-41 materials containing transition metals: synthesis and characterization. *Appl. Catal., A* **2004**, *272*, 257−266.
(62) Vanelderen, P.; Snyder, B. E. R.; Tsai, M.-L.; Hadt, R. G.; Vancauwenbergh, J.; Coussens, O.; Schoonheydt, R. A.; Sels, B. F.; Solomon, E. I. Spectroscopic Definition of the Copper Active Sites in Mordenite: Selective Methane Oxidation. *J. Am. Chem. Soc.* **2015**, *137*, 6383−6392.
(63) Beznis, N. V.; Weckhuysen, B. M.; Bitter, J. H. Cu-ZSM-5 Zeolites for the Formation of Methanol from Methane and Oxygen: Probing the Active Sites and Spectator Species. *Catal. Lett.* **2010**, *138*, 14−22.
(64) Giordanino, F.; Vennestrøm, P. N. R.; Lundegaard, L. F.; Stappen, F. N.; Mossin, S.; Beato, P.; Bordiga, S.; Lamberti, C. Characterization of Cu-exchanged SSZ-13: a comparative FTIR, UV-Vis, and EPR study with Cu-ZSM-5 and Cu-β with similar Si/Al and Cu/Al ratios. *Dalton Trans.* **2013**, *42*, 12741−12761.
(65) Kitajima, N.; Fujisawa, K.; Fujimoto, C.; Morooka, Y.; Hashimoto, S.; Kitagawa, T.; Toriumi, K.; Tatsumi, K.; Nakamura, A. A new model for dioxygen binding in hemocyanin. Synthesis, characterization, and molecular structure of the μ- η^2: η^2 peroxo dinuclear copper(II) complexes, $[Cu(HB(3,5\text{-}R2pz)_3)]_2(O_2)$ (R= isopropyl and Ph). *J. Am. Chem. Soc.* **1992**, *114*, 1277−1291.
(66) Vanelderen, P.; Vancauwenbergh, J.; Sels, B. F.; Schoonheydt, R. A. Coordination chemistry and reactivity of copper in zeolites. *Coord. Chem. Rev.* **2013**, *257*, 483−494.
(67) Delabie, A.; Pierloot, K.; Groothaert, Marijke H.; Schoonheydt, Robert A.; Vanquickenborne, Luc G. The Coordination of CuII in Zeolites − Structure and Spectroscopic Properties. *Eur. J. Inorg. Chem.* **2002**, *2002*, 515−530.
(68) Groothaert, M. H.; Pierloot, K.; Delabie, A.; Schoonheydt, R. A. Identification of Cu(ii) coordination structures in Cu-ZSM-5, based on a DFT/ab initio assignment of the EPR spectra. *Phys. Chem. Chem. Phys.* **2003**, *5*, 2135−2144.
(69) Deka, U.; Lezcano-Gonzalez, I.; Weckhuysen, B. M.; Beale, A. M. Local Environment and Nature of Cu Active Sites in Zeolite-Based Catalysts for the Selective Catalytic Reduction of NOx. *ACS Catal.* **2013**, *3*, 413−427.
(70) Dědeček, J.; Bortnovsky, O.; Vondrová, A.; Wichterlová, B. Catalytic Activity of Cu-Beta Zeolite in NO Decomposition: Effect of Copper and Aluminium Distribution. *J. Catal.* **2001**, *200*, 160−170.
(71) Brandenberger, S.; Kröcher, O.; Tissler, A.; Althoff, R. The determination of the activities of different iron species in Fe-ZSM-5 for SCR of NO by NH_3. *Appl. Catal., B* **2010**, *95*, 348−357.
(72) Sádovská, G.; Tabor, E.; Bernauer, M.; Sazama, P.; Fíla, V.; Kmječ, T.; Kohout, J.; Závěta, K.; Tokarová, V.; Sobalík, Z. FeO_x/Al_2O_3 catalysts for high-temperature decomposition of N_2O under conditions of NH_3 oxidation in nitric acid production. *Catal. Sci. Technol.* **2018**, *8*, 2841−2852.
(73) Chernyshova, I. V.; Ponnurangam, S.; Somasundaran, P. On the origin of an unusual dependence of (bio)chemical reactivity of ferric hydroxides on nanoparticle size. *Phys. Chem. Chem. Phys.* **2010**, *12*, 14045−14056.
(74) Bordiga, S.; Buzzoni, R.; Geobaldo, F.; Lamberti, C.; Giamello, E.; Zecchina, A.; Leofanti, G.; Petrini, G.; Tozzola, G.; Vlaic, G. Structure and reactivity of framework and extraframework iron in Fe-silicalite as investigated by spectroscopic and physicochemical methods. *J. Catal.* **1996**, *158*, 486−501.
(75) Pirngruber, G. D.; Roy, P. K.; Prins, R. On determining the nuclearity of iron sites in Fe-ZSM-5 - A critical evaluation. *Phys. Chem. Chem. Phys.* **2006**, *8*, 3939−3950.
(76) Čapek, L.; Kreibich, V.; Dědeček, J.; Grygar, T.; Wichterlová, B.; Sobalík, Z.; Martens, J. A.; Brosius, R.; Tokarová, V. Analysis of Fe species in zeolites by UV−VIS−NIR, IR spectra and voltammetry. Effect of preparation, Fe loading and zeolite type. *Microporous Mesoporous Mater.* **2005**, *80*, 279−289.
(77) Dubkov, K. A.; Ovanesyan, N. S.; Shteinman, A. A.; Starokon, E. V.; Panov, G. I. Evolution of Iron States and Formation of α-Sites upon Activation of FeZSM-5 Zeolites. *J. Catal.* **2002**, *207*, 341−352.
(78) Tabor, E.; Závěta, K.; Sathu, N. K.; Vondrová, A.; Sazama, P.; Sobalík, Z. N_2O decomposition over Fe-FER: A Mössbauer study of the active sites. *Catal. Today* **2011**, *175*, 238−244.
(79) Fierro, G.; Moretti, G.; Ferraris, G.; Andreozzi, G. B. A Mössbauer and structural investigation of Fe-ZSM-5 catalysts: Influence of Fe oxide nanoparticles size on the catalytic behaviour for the NO-SCR by C_3H_8. *Appl. Catal., B* **2011**, *102*, 215−223.
(80) Maier, S. M.; Jentys, A.; Metwalli, E.; Müller-Buschbaum, P.; Lercher, J. A. Determination of the redox processes in FeBEA catalysts in NH3-SCR reaction by Mössbauer and X-ray absorption spectroscopy. *J. Phys. Chem. Lett.* **2011**, *2*, 950−955.
(81) Tabor, E.; Sádovská, G.; Bernauer, M.; Sazama, P.; Nováková, J.; Fíla, V.; Kmječ, T.; Kohout, J.; Závěta, K.; Sobalík, Z. Feasibility of application of iron zeolites for high-temperature decomposition of N_2O under real conditions of the technology for nitric acid production. *Appl. Catal., B* **2019**, *240*, 358−366.
(82) Sádovská, G.; Tabor, E.; Sazama, P.; Lhotka, M.; Bernauer, M.; Sobalík, Z. High temperature performance and stability of Fe-FER catalyst for N_2O decomposition. *Catal. Commun.* **2017**, *89*, 133−137.
(83) Sobalik, Z.; Novakova, J.; Dedecek, J.; Sathu, N. K.; Tabor, E.; Sazama, P.; Stastny, P.; Wichterlova, B. Tailoring of Fe-ferrierite for N_2O decomposition: On the decisive role of framework Al distribution for catalytic activity of Fe species in Fe-ferrierite. *Microporous Mesoporous Mater.* **2011**, *146*, 172−183.
(84) Guczi, L.; Lázár, K. Mössbauer spectroscopy in heterogeneous catalysis: A brief overview and recent study on paramagnetic features detected in catalytic centres of Fe-ZSM-5. *React. Kinet. Catal. Lett.* **2009**, *96*, 335−343.
(85) Wang, A.; Wang, Y.; Walter, E. D.; Kukkadapu, R. K.; Guo, Y.; Lu, G.; Weber, R. S.; Wang, Y.; Peden, C. H. F.; Gao, F. Catalytic N_2O decomposition and reduction by NH_3 over Fe/Beta and Fe/SSZ-13 catalysts. *J. Catal.* **2018**, *358*, 199−210.
(86) Kurtz, D. M. Oxo- and hydroxo-bridged diiron complexes: a chemical perspective on a biological unit. *Chem. Rev.* **1990**, *90*, 585−606.
(87) Hansen, N.; Heyden, A.; Bell, A. T.; Keil, F. J. A Reaction Mechanism for the Nitrous Oxide Decomposition on Binuclear Oxygen Bridged Iron Sites in Fe-ZSM-5. *J. Phys. Chem. C* **2007**, *111*, 2092−2101.

(88) Sun, K.; Xia, H.; Feng, Z.; van Santen, R.; Hensen, E.; Li, C. Active sites in Fe/ZSM-5 for nitrous oxide decomposition and benzene hydroxylation with nitrous oxide. *J. Catal.* **2008**, *254*, 383−396.
(89) Yuranov, I.; Bulushev, D. A.; Renken, A.; Kiwi-Minsker, L. Benzene hydroxylation over FeZSM-5 catalysts: which Fe sites are active? *J. Catal.* **2004**, *227*, 138−147.
(90) Kim, J.; Jentys, A.; Maier, S. M.; Lercher, J. A. Characterization of Fe-Exchanged BEA Zeolite Under NH_3 Selective Catalytic Reduction Conditions. *J. Phys. Chem. C* **2013**, *117*, 986−993.
(91) Merkx, M.; Kopp, D. A.; Sazinsky, M. H.; Blazyk, J. L.; Muanďller, J.; Lippard, S. J. Dioxygen activation and methane hydroxylation by soluble methane monooxygenase: A tale of two irons and three proteins. *Angew. Chem., Int. Ed.* **2001**, *40*, 2782−2807.
(92) Rosenzweig, A. C.; Frederick, C. A.; Lippard, S. J.; Nordlund, P. Crystal structure of a bacterial non-haem iron hydroxylase that catalyses the biological oxidation of methane. *Nature* **1993**, *366*, 537−543.
(93) Solomon, E. I.; Heppner, D. E.; Johnston, E. M.; Ginsbach, J. W.; Cirera, J.; Qayyum, M.; Kieber-Emmons, M. T.; Kjaergaard, C. H.; Hadt, R. G.; Tian, L. Copper active sites in biology. *Chem. Rev.* **2014**, *114*, 3659−3853.
(94) Palagin, D.; Knorpp, A. J.; Pinar, A. B.; Ranocchiari, M.; van Bokhoven, J. A. Assessing the relative stability of copper oxide clusters as active sites of a CuMOR zeolite for methane to methanol conversion: size matters? *Nanoscale* **2017**, *9*, 1144−1153.
(95) Alayon, E. M. C.; Nachtegaal, M.; Bodi, A.; Ranocchiari, M.; van Bokhoven, J. A. Bis(μ-oxo) versus mono(μ-oxo)dicopper cores in a zeolite for converting methane to methanol: an in situ XAS and DFT investigation. *Phys. Chem. Chem. Phys.* **2015**, *17*, 7681−7693.
(96) Pannov, G. I.; Sobolev, V. I.; Kharitonov, A. S. The Role of Iron in N_2O Decomposition on ZSM-5 Zeolite and Reactivity of the Surface Oxygen Formed. *J. Mol. Catal.* **1990**, *61*, 85−97.
(97) Snyder, B. E. R.; Vanelderen, P.; Bols, M. L.; Hallaert, S. D.; Bottger, L. H.; Ungur, L.; Pierloot, K.; Schoonheydt, R. A.; Sels, B. F.; Solomon, E. I. The active site of low-temperature methane hydroxylation in iron-containing zeolites. *Nature* **2016**, *536*, 317−332.
(98) Sharma, V. K. Ferrate(VI) and ferrate(V) oxidation of organic compounds: Kinetics and mechanism. *Coord. Chem. Rev.* **2013**, *257*, 495−510.
(99) Li, G.; Pidko, E. A.; van Santen, R. A.; Li, C.; Hensen, E. J. M. Stability of Extraframework Iron-Containing Complexes in ZSM-5 Zeolite. *J. Phys. Chem. C* **2013**, *117*, 413−426.
(100) Kulkarni, A. R.; Zhao, Z. J.; Siahrostami, S.; Norskov, J. K.; Studt, F. Cation-exchanged zeolites for the selective oxidation of methane to methanol. *Catal. Sci. Technol.* **2018**, *8*, 114−123.
(101) Arvidsson, A. A.; Zhdanov, V. P.; Carlsson, P. A.; Gronbeck, H.; Hellman, A. Metal dimer sites in ZSM-5 zeolite for methane-to-methanol conversion from first-principles kinetic modelling: is the [Cu-O-Cu](2+) motif relevant for Ni, Co, Fe, Ag, and Au? *Catal. Sci. Technol.* **2017**, *7*, 1470−1477.
(102) Sushkevich, V. L.; Palagin, D.; Ranocchiari, M.; van Bokhoven, J. A. Selective anaerobic oxidation of methane enables direct synthesis of methanol. *Science* **2017**, *356*, 523−527.
(103) Hammond, C.; Forde, M. M.; Ab Rahim, M. H.; Thetford, A.; He, Q.; Jenkins, R. L.; Dimitratos, N.; Lopez-Sanchez, J. A.; Dummer, N. F.; Murphy, D. M.; Carley, A. F.; Taylor, S. H.; Willock, D. J.; Stangland, E. E.; Kang, J.; Hagen, H.; Kiely, C. J.; Hutchings, G. J. Direct Catalytic Conversion of Methane to Methanol in an Aqueous Medium by using Copper-Promoted Fe-ZSM-5. *Angew. Chem., Int. Ed.* **2012**, *51*, 5129−5133.
(104) Hammond, C.; Dimitratos, N.; Jenkins, R. L.; Lopez-Sanchez, J. A.; Kondrat, S. A.; ab Rahim, M. H.; Forde, M. M.; Thetford, A.; Taylor, S. H.; Hagen, H.; Stangland, E. E.; Kang, J. H.; Moulijn, J. M.; Willock, D. J.; Hutchings, G. J. Elucidation and Evolution of the Active Component within Cu/Fe/ZSM-5 for Catalytic Methane Oxidation: From Synthesis to Catalysis. *ACS Catal.* **2013**, *3*, 689−699.
(105) Hammond, C.; Jenkins, R. L.; Dimitratos, N.; Lopez-Sanchez, J. A.; ab Rahim, M. H.; Forde, M. M.; Thetford, A.; Murphy, D. M.; Hagen, H.; Stangland, E. E.; Moulijn, J. M.; Taylor, S. H.; Willock, D. J.; Hutchings, G. J. Catalytic and Mechanistic Insights of the Low-Temperature Selective Oxidation of Methane over Cu-Promoted Fe-ZSM-5. *Chem. − Eur. J.* **2012**, *18*, 15735−15745.
(106) Snyder, B. E. R.; Vanelderen, P.; Bols, M. L.; Hallaert, S. D.; Bottger, L. H.; Ungur, L.; Pierloot, K.; Schoonheydt, R. A.; Sels, B. F.; Solomon, E. I. The active site of low-temperature methane hydroxylation in iron-containing zeolites. *Nature* **2016**, *536*, 317−321.
(107) Dubkov, K. A.; Sobolev, V. I.; Panov, G. I. Low-temperature oxidation of methane to methanol on FeZSM-5 zeolite. *Kinet. Catal.* **1998**, *39*, 72−79.
(108) Bols, M. L.; Hallaert, S. D.; Snyder, B. E. R.; Devos, J.; Plessers, D.; Rhoda, H. M.; Dusselier, M.; Schoonheydt, R. A.; Pierloot, K.; Solomon, E. I.; Sels, B. F. Spectroscopic Identification of the alpha-Fe/alpha-O Active Site in Fe-CHA Zeolite for the Low-Temperature Activation of the Methane C−H Bond. *J. Am. Chem. Soc.* **2018**, *140*, 12021−12032.
(109) Snyder, B. E. R.; Vanelderen, P.; Bols, M. L.; Hallaert, S. D.; Bottger, L. H.; Ungur, L.; Pierloot, K.; Schoonheydt, R. A.; Sels, B. F.; Solomon, E. I. The active site of low-temperature methane hydroxylation in iron-containing zeolites. *Nature* **2016**, *536*, 317−332.
(110) Sazama, P.; Mokrzycki, L.; Wichterlova, B.; Vondrova, A.; Pilar, R.; Dedecek, J.; Sklenak, S.; Tabor, E. Unprecedented propane-SCR-NO_x activity over template-free synthesized Al-rich Co-BEA* zeolite. *J. Catal.* **2015**, *332*, 201−211.
(111) Wang, G.; Chen, W.; Huang, L.; Liu, Z.; Sun, X.; Zheng, A. Reactivity descriptors of diverse copper-oxo species on ZSM-5 zeolite towards methane activation. *Catal. Today* **2019**, *338*, 108−116.
(112) Bols, M. L.; Hallaert, S. D.; Snyder, B. E. R.; Devos, J.; Plessers, D.; Rhoda, H. M.; Dusselier, M.; Schoonheydt, R. A.; Pierloot, K.; Solomon, E. I.; Sels, B. F. Spectroscopic Identification of the α-Fe/α-O Active Site in Fe-CHA Zeolite for the Low-Temperature Activation of the Methane C−H Bond. *J. Am. Chem. Soc.* **2018**, *140*, 12021−12032.
(113) Yang, W. L.; Li, D.; Xu, D. M.; Wang, X. Y. Effect of CeO_2 preparation method and Cu loading on CuO/CeO_2 catalysts for methane combustion. *J. Nat. Gas Chem.* **2009**, *18*, 458−466.
(114) Popescu, I.; Tanchoux, N.; Tichit, D.; Marcu, I. C. Total oxidation of methane over supported CuO: Influence of the MgxAlyO support. *Appl. Catal., A* **2017**, *538*, 81−90.
(115) Kaddouri, A.; Dupont, N.; Gelin, P.; Delichere, P. Methane Combustion Over Copper Chromites Catalysts Prepared by the Sol-Gel Process. *Catal. Lett.* **2011**, *141*, 1581−1589.
(116) Águila, G.; Gracia, F.; Cortes, J.; Araya, P. Effect of copper species and the presence of reaction products on the activity of methane oxidation on supported CuO catalysts. *Appl. Catal., B* **2008**, *77*, 325−338.
(117) Artizzu, P.; Garbowski, E.; Primet, M.; Brulle, Y.; Saint-Just, J. Catalytic combustion of methane on aluminate-supported copper oxide. *Catal. Today* **1999**, *47*, 83−93.
(118) Al-Aani, H. M. S.; Iro, E.; Chirra, P.; Fechete, I.; Badea, M.; Negrilă, C.; Popescu, I.; Olea, M.; Marcu, I.-C. $Cu_xCeMgAlO$ mixed oxide catalysts derived from multicationic LDH precursors for methane total oxidation. *Appl. Catal., A* **2019**, *586*, No. 117215.
(119) Răciulete, M.; Layrac, G.; Tichit, D.; Marcu, I. C. Comparison of Cu_xZnAlO mixed oxide catalysts derived from multicationic and hybrid LDH precursors for methane total oxidation. *Appl. Catal., A* **2014**, *477*, 195−204.
(120) Zhang, L.; Zhang, Y.; Dai, H. X.; Deng, J. G.; Wei, L.; He, H. Hydrothermal synthesis and catalytic performance of single-crystalline $La_{2-x}Sr_xCuO_4$ for methane oxidation. *Catal. Today* **2010**, *153*, 143−149.
(121) Sánchez, J. J.; Lopez-Haro, M.; Hernandez-Garrido, J. C.; Blanco, G.; Cauqui, M. A.; Rodriguez-Izquierdo, J. M.; Perez-Omil, J. A.; Calvino, J. J.; Yeste, M. P. An atomically efficient, highly stable and redox active $Ce_{0.5}Tb_{0.5}O_x$ (3% mol.)/MgO catalyst for total oxidation of methane. *J. Mater. Chem. A* **2019**, *7*, 8993−9003.
(122) Vickers, S. M.; Gholami, R.; Smith, K. J.; MacLachlan, M. J. Mesoporous Mn- and La-Doped Cerium Oxide/Cobalt Oxide Mixed Metal Catalysts for Methane Oxidation. *ACS Appl. Mater. Interfaces* **2015**, *7*, 11460−11466.
(123) Urdă, A.; Popescu, I.; Cacciaguerra, T.; Tanchoux, N.; Tichit, D.; Marcu, I. C. Total oxidation of methane over rare earth cation-

containing mixed oxides derived from LDH precursors. *Appl. Catal., A* **2013**, *464−465*, 20−27.
(124) Arai, H.; Yamada, T.; Eguchi, K.; Seiyama, T. Catalytic Combustion of Methane over Various Perovskite-Type Oxides. *Appl. Catal.* **1986**, *26*, 265−276.
(125) Arandiyan, H.; Dai, H. X.; Deng, J. G.; Liu, Y. X.; Bai, B. Y.; Wang, Y.; Li, X. W.; Xie, S. H.; Li, J. H. Three-dimensionally ordered macroporous $La_{0.6}Sr_{0.4}MnO_3$ with high surface areas: Active catalysts for the combustion of methane. *J. Catal.* **2013**, *307*, 327−339.
(126) Taguchi, H.; Nakade, K.; Yosinaga, M.; Kato, M.; Hirota, K. Methane oxidation on perovskite-type $Ca(Mn_{1-x}Ti_x)O_3$-delta. *J. Am. Ceram. Soc.* **2008**, *91*, 308−310.
(127) Wang, Y. G.; Ren, J. W.; Wang, Y. Q.; Zhang, F. Y.; Liu, X. H.; Guo, Y.; Lu, G. Z. Nanocasted synthesis of mesoporous $LaCoO_3$ perovskite with extremely high surface area and excellent activity in methane combustion. *J. Phys. Chem. C* **2008**, *112*, 15293−15298.
(128) Huang, F.; Wang, X. D.; Wang, A. Q.; Xu, J. M.; Zhang, T. A two-step synthesis of Fe-substituted hexaaluminates with enhanced surface area and activity in methane catalytic combustion. *Catal. Sci. Technol.* **2016**, *6*, 4962−4969.
(129) Hu, R. S.; Bai, Y. Q.; Du, H. Y.; Zhang, H. M.; Du, Y. F.; Zhang, J. E.; Zhou, Q. H. Surface structure and catalytic performance of Sr-doped La_2NiAlO_6 double perovskite catalysts for methane combustion. *J. Rare Earths* **2015**, *33*, 1284−1292.
(130) Arandiyan, H.; Scott, J.; Wang, Y.; Dai, H. X.; Sun, H. Y.; Amal, R. Meso-Molding Three-Dimensional Macroporous Perovskites: A New Approach to Generate High-Performance Nanohybrid Catalysts. *ACS Appl. Mater. Interfaces* **2016**, *8*, 2457−2463.
(131) Nie, L. H.; Wang, J.; Tan, Q. In-situ preparation of macro/mesoporous $NiO/LaNiO_3$ pervoskite composite with enhanced methane combustion performance. *Catal. Commun.* **2017**, *97*, 1−4.
(132) Xiao, T. C.; Ji, S. F.; Wang, H. T.; Coleman, K. S.; Green, M. L. H. Methane combustion over supported cobalt catalysts. *J. Mol. Catal. A: Chem.* **2001**, *175*, 111−123.
(133) Chen, M.; Fan, L. P.; Zheng, X. M. Effect of novel supporter on catalytic combustion of methane. *J. Rare Earths* **2006**, *24*, 447−450.
(134) Hu, J.; Chu, W.; Shi, L. Effects of carrier and Mn loading on supported manganese oxide catalysts for catalytic combustion of methane. *J. Nat. Gas Chem.* **2008**, *17*, 159−164.
(135) Okumura, K.; Shinohara, E.; Niwa, M. Pd loaded on high silica beta support active for the total oxidation of diluted methane in the presence of water vapor. *Catal. Today* **2006**, *117*, 577−583.
(136) Petrov, A. W.; Ferri, D.; Krocher, O.; van Bokhoven, J. A. Design of Stable Palladium-Based Zeolite Catalysts for Complete Methane Oxidation by Postsynthesis Zeolite Modification. *ACS Catal.* **2019**, *9*, 2303−2312.
(137) Friberg, I.; Sadokhina, N.; Olsson, L. The effect of Si/Al ratio of zeolite supported Pd for complete CH_4 oxidation in the presence of water vapor and SO_2. *Appl. Catal., B* **2019**, *250*, 117−131.
(138) M'Ramadj, O.; Li, D.; Wang, X. Y.; Zhang, B.; Lu, G. Z. Role of acidity of catalysts on methane combustion over Pd/ZSM-5. *Catal. Commun.* **2007**, *8*, 880−884.
(139) Roth, D.; Gelin, P.; Tena, E.; Primet, M. Combustion of methane at low temperature over Pd and Pt catalysts supported on Al_2O_3, SnO_2 and Al_2O_3-grafted SnO_2. *Top. Catal.* **2001**, *16/17*, 77−82.
(140) Lin, W.; Lin, L.; Zhu, Y. X.; Xie, Y. C.; Scheurell, K.; Kemnitz, E. Novel Pd/TiO_2-Al_2O_3 catalysts for methane total oxidation at low temperature and their O-18-isotope exchange behavior. *Chin. J. Chem.* **2005**, *23*, 1333−1338.
(141) Corro, G.; Torralba, R.; Pal, U.; Olivares-Xometl, O.; Fierro, J. L. G. Total Oxidation of Methane over Pt/Cr_2O_3 Catalyst at Low Temperature: Effect of Pt-0-Ptx+ Dipoles at the Metal-Support Interface. *J. Phys. Chem. C* **2019**, *123*, 2882−2893.
(142) Miao, S. J.; Deng, Y. Q. Au-Pt/Co_3O_4 catalyst for methane combustion. *Appl. Catal., B* **2001**, *31*, L1−L4.
(143) Liotta, L. F.; Di Carlo, G.; Longo, A.; Pantaleo, G.; Venezia, A. M. Support effect on the catalytic performance of Au/Co_3O_4-CeO_2 catalysts for CO and CH_4 oxidation. *Catal. Today* **2008**, *139*, 174−179.
(144) Zhang, Y. J.; Deng, J. G.; Zhang, L.; Dai, H. X. Preparation and catalytic performance of Fe-SBA-15 and FeO_x/SBA-15 for toluene combustion. *Chin. Sci. Bull.* **2014**, *59*, 3993−4002.
(145) Boycheva, S.; Zgureva, D.; Vaclavikova, M.; Kalvachev, Y.; Lazarova, H.; Popova, M. Studies on non-modified and copper-modified coal ash zeolites as heterogeneous catalysts for VOCs oxidation. *J. Hazard. Mater.* **2019**, *361*, 374−382.
(146) Nogueira, F. G. E.; Lopes, J. H.; Silva, A. C.; Lago, R. M.; Fabris, J. D.; Oliveira, L. C. A. Catalysts based on clay and iron oxide for oxidation of toluene. *Appl. Clay Sci.* **2011**, *51*, 385−389.
(147) Soylu, G. S. P.; Ozcelik, Z.; Boz, I. Total oxidation of toluene over metal oxides supported on a natural clinoptilolite-type zeolite. *Chem. Eng. J.* **2010**, *162*, 380−387.
(148) Li, D.; Li, C. S.; Suzuki, K. Catalytic oxidation of VOCs over Al- and Fe-pillared montmorillonite. *Appl. Clay Sci.* **2013**, *77-78*, 56−60.
(149) Carrillo, A. M.; Carriazo, J. G. Cu and Co oxides supported on halloysite for the total oxidation of toluene. *Appl. Catal., B* **2015**, *164*, 443−452.
(150) Szegedi, Á.; Popova, M.; Lazar, K.; Klebert, S.; Drotar, E. Impact of silica structure of copper and iron-containing SBA-15 and SBA-16 materials on toluene oxidation. *Microporous Mesoporous Mater.* **2013**, *177*, 97−104.
(151) Liotta, L. F. Catalytic oxidation of volatile organic compounds on supported noble metals. *Appl. Catal., B* **2010**, *100*, 403−412.
(152) Chen, C. Y.; Zhu, J.; Chen, F.; Meng, X. J.; Zheng, X. M.; Gao, X. H.; Xiao, F. S. Enhanced performance in catalytic combustion of toluene over mesoporous Beta zeolite-supported platinum catalyst. *Appl. Catal., B* **2013**, *140−141*, 199−205.
(153) Chen, C. Y.; Wu, Q. M.; Chen, F.; Zhang, L.; Pan, S. X.; Bian, C. Q.; Zheng, X. M.; Meng, X. J.; Xiao, F. S. Aluminium-rich Beta zeolite-supported platinum nanoparticles for the low-temperature catalytic removal of toluene. *J. Mater. Chem. A* **2015**, *3*, 5556−5562.
(154) Chen, C. Y.; Wang, X.; Zhang, J.; Bian, C. Q.; Pan, S. X.; Chen, F.; Meng, X. J.; Zheng, X. M.; Gao, X. H.; Xiao, F. S. Superior performance in catalytic combustion of toluene over mesoporous ZSM-5 zeolite supported platinum catalyst. *Catal. Today* **2015**, *258*, 190−195.
(155) Chen, C. Y.; Wang, X.; Zhang, J.; Pan, S. X.; Bian, C. Q.; Wang, L.; Chen, F.; Meng, X. J.; Zheng, X. M.; Gao, X. H.; Xiao, F. S. Superior Performance in Catalytic Combustion of Toluene over KZSM-5 Zeolite Supported Platinum Catalyst. *Catal. Lett.* **2014**, *144*, 1851−1859.
(156) Zhang, J. Y.; Rao, C.; Peng, H. G.; Peng, C.; Zhang, L.; Xu, X. L.; Liu, W. M.; Wang, Z.; Zhang, N.; Wang, X. Enhanced toluene combustion performance over Pt loaded hierarchical porous MOR zeolite. *Chem. Eng. J.* **2018**, *334*, 10−18.
(157) O'Malley, A.; Hodnett, B. K. The influence of volatile organic compound structure on conditions required for total oxidation. *Catal. Today* **1999**, *54*, 31−38.
(158) Alifanti, M.; Florea, M.; Somacescu, S.; Parvulescu, V. I. Supported perovskites for total oxidation of toluene. *Appl. Catal., B* **2005**, *60*, 33−39.
(159) Rousseau, S.; Loridant, S.; Delichere, P.; Boreave, A.; Deloume, J. P.; Vernoux, P. $La_{(1-x)}Sr_xCo_{(1-y)}Fe_yO_3$ perovskites prepared by sol-gel method: Characterization and relationships with catalytic properties for total oxidation of toluene. *Appl. Catal., B* **2009**, *88*, 438−447.
(160) Florea, M.; Alifanti, M.; Parvulescu, V. I.; Mihaila-Tarabasanu, D.; Diamandescu, L.; Feder, M.; Negrila, C.; Frunza, L. Total oxidation of toluene on ferrite-type catalysts. *Catal. Today* **2009**, *141*, 361−366.
(161) Gennequin, C.; Cousin, R.; Lamonier, J. F.; Siffert, S.; Aboukais, A. Toluene total oxidation over Co supported catalysts synthesised using memory effect" of Mg-Al hydrotalcite. *Catal. Commun.* **2008**, *9*, 1639−1643.
(162) Palacio, L. A.; Velasquez, J.; Echavarria, A.; Faro, A.; Ribeiro, F. R.; Ribeiro, M. F. Total oxidation of toluene over calcined trimetallic hydrotalcites type catalysts. *J. Hazard. Mater.* **2010**, *177*, 407−413.
(163) Dula, R.; Janik, R.; Machej, T.; Stoch, J.; Grabowski, R.; Serwicka, E. M. Mn-containing catalytic materials for the total

combustion of toluene: The role of Mn localisation in the structure of LDH precursor. *Catal. Today* **2007**, *119*, 327−331.
(164) Genty, E.; Brunet, J.; Poupin, C.; Casale, S.; Capelle, S.; Massiani, P.; Siffert, S.; Cousin, R. Co-Al Mixed Oxides Prepared via LDH Route Using Microwaves or Ultrasound: Application for Catalytic Toluene Total Oxidation. *Catalysts* **2015**, *5*, 851−867.
(165) Piumetti, M.; Fino, D.; Russo, N. Mesoporous manganese oxides prepared by solution combustion synthesis as catalysts for the total oxidation of VOCs. *Appl. Catal., B* **2015**, *163*, 277−287.
(166) Qu, Z. P.; Gao, K.; Fu, Q.; Qin, Y. Low-temperature catalytic oxidation of toluene over nanocrystal-like Mn-Co oxides prepared by two-step hydrothermal method. *Catal. Commun.* **2014**, *52*, 31−35.
(167) Del Angel, G.; Padilla, J. M.; Cuauhtemoc, I.; Navarrete, J. Toluene combustion on gamma-Al_2O_3-CeO_2 catalysts prepared from boehmite and cerium nitrate. *J. Mol. Catal. A: Chem.* **2008**, *281*, 173−178.
(168) Pozan, G. S. Effect of support on the catalytic activity of manganese oxide catalyts for toluene combustion. *J. Hazard. Mater.* **2012**, *221−222*, 124−130.
(169) Ma, W. J.; Huang, Q.; Xu, Y.; Chen, Y. W.; Zhu, S. M.; Shen, S. B. Catalytic combustion of toluene over Fe-Mn mixed oxides supported on cordierite. *Ceram. Int.* **2013**, *39*, 277−281.
(170) Morales, M. R.; Barbero, B. P.; Cadus, L. E. Total oxidation of ethanol and propane over Mn-Cu mixed oxide catalysts. *Appl. Catal., B* **2006**, *67*, 229−236.
(171) Delimaris, D.; Ioannides, T. VOC oxidation over CuO-CeO_2 catalysts prepared by a combustion method. *Appl. Catal., B* **2009**, *89*, 295−302.
(172) Larsson, P. O.; Andersson, A. Oxides of copper, ceria promoted copper, manganese and copper manganese on Al_2O_3 for the combustion of CO, ethyl acetate and ethanol. *Appl. Catal., B* **2000**, *24*, 175−192.
(173) Pecchi, G.; Reyes, P.; Zamora, R.; Cadus, L. E.; Fierro, J. L. G. Surface properties and performance for VOCs combustion of $LaFe_{1-y}Ni_yO_3$ perovskite oxides. *J. Solid State Chem.* **2008**, *181*, 905−912.
(174) Bastos, S. S. T.; Orfao, J. J. M.; Freitas, M. M. A.; Pereira, M. F. R.; Figueiredo, J. L. Manganese oxide catalysts synthesized by exotemplating for the total oxidation of ethanol. *Appl. Catal., B* **2009**, *93*, 30−37.
(175) Zhang, Z.; Jiang, Z.; Shangguan, W. Low-temperature catalysis for VOCs removal in technology and application: A state-of-the-art review. *Catal. Today* **2016**, *264*, 270−278.
(176) Everaert, K.; Baeyens, J. Catalytic combustion of volatile organic compounds. *J. Hazard. Mater.* **2004**, *109*, 113−139.
(177) Kamal, M. S.; Razzak, S. A.; Hossain, M. M. Catalytic oxidation of volatile organic compounds (VOCs) − A review. *Atmos. Environ.* **2016**, *140*, 117−134.

https://dx.doi.org/10.1021/acscatal.9b05431
ACS Catal. 2020, 10, 3984−4002